https://doi.org/10.5194/wes-2026-147
Preprint. Discussion started: 10 September 2026

eawe european academy of wind energy
Open Access WIND ENERGY SCIENCE DISCUSSIONS

Sensitivity of Offshore Wind Farm Wakes and Ocean Coupling to Vertical Resolution in the Stable Marine Boundary Layer

Adam Ayouche[1], Baylor Fox-Kemper[1], Nathan Laxague[2], and Nicholas Pizzo[3]

[1]Department of Earth, Environmental, and Planetary Sciences, Brown University, Providence, RI, USA
[2]Department of Mechanical Engineering, University of New Hampshire, Durham, NH, USA
[3]Graduate School of Oceanography, University of Rhode Island, Narragansett, RI, USA

Correspondence: Adam Ayouche (aayouche@brown.edu)

Abstract.

Offshore wind farms in the Southern New England lease area frequently operate within a persistently stable marine atmospheric boundary layer (MABL) during spring, when cold shelf waters beneath warm continental air suppress convective mixing and maintain a shallow planetary boundary layer height (PBLH) well below turbine hub height. Here we quantify the sensitivity of wind farm simulations to vertical resolution under these heavily stratified conditions. Our ensemble of WRF-Fitch mesoscale simulations of a large-scale offshore wind farm during a stratified period (2–8 May 2018) spans five vertical grid configurations, labeled by their first-layer thickness (Δz = 5–100 m), which place between 27 and 2 model levels within the 30–246 m rotor swept zone, and two ABL schemes (MYNN2 and YSU), coupled to a one-dimensional slab ocean to diagnose first-order air-sea interactions. The simulated mean PBLH of 92–118 m places 59–72% of the rotor above the boundary-layer top, where strong stratification suppresses the turbulent redistribution of the wake and concentrates almost all of the shear across the disk below hub height. Hub-height wind speed and friction velocity are robustly represented for $\Delta z \leq 50$ m, departing by less than 1.2% and 1% respectively in MYNN2, but coarser grids (resembling operational system resolution) fail to resolve the sharp stable inversion: Δz = 100 m overestimates PBLH by 87% with MYNN2 and 22% with YSU. Richardson extrapolation over the three finest grids shows most diagnostics to be effectively grid-converged at the reference resolution, but assigns PBLH a grid convergence index of about 13%, reflecting its nature as a threshold diagnostic evaluated on model levels.

Crucially, the hub-height wake deficit and its downstream structure remain robust across vertical resolutions, so this 13% PBLH error chiefly compromises PBLH-based diagnostics rather than the simulated wake and surface stresses. The time-mean wake deficit peaks at -3.2 m s^{-1} at the cluster core and falls below 0.5 and 0.1 m s^{-1} at 81 and 136 km downstream, driving a spatial PBLH dipole (a $+90$ m in-farm deepening and a -24 m downstream undershoot that recovers within 23 km), the former being consistent with recent observations on land. The ocean responds to the reduced wind stress (13.5%) with a mixed-layer shoaling of 1.26 m (9.2%) within the farm footprint, a sea-surface skin warming peaking at $+0.32$ °C, and an upward turbulent heat-flux anomaly of 2.23 W m^{-2} (10.7%) in the farm zone, reaching 3.18 W m^{-2} some 47 km downwind of the stress minimum, consistent in sign and magnitude with fully coupled simulations of the same region. The air-sea fluxes and the mixed-layer response show no ordered dependence on resolution across the four finest grids, although the coarsest, operational-like resolution exaggerates every term.

https://doi.org/10.5194/wes-2026-147
Preprint. Discussion started: 10 September 2026

eawe european academy of wind energy
Open Access
WIND ENERGY SCIENCE
DISCUSSIONS

These results establish that while the spatial structure of wake-induced atmospheric and oceanic perturbations is robust to vertical resolution once converged, the precise quantification of PBLH-dependent wake dynamics requires at least eight model levels within the rotor layer, corresponding here to $\Delta z \leq 25$ m. The ERA5 reanalysis that provides the boundary conditions for these simulations places eight levels within the same layer, so its vertical grid sits at the threshold identified here; regional forecast systems with coarser near-surface grids would not resolve it. Vertical refinement beyond this point is bounded by the horizontal discretization: at 1.5 km spacing the boundary-layer scheme remains a one-dimensional column closure, and further progress requires relaxing that assumption toward 3D turbulence resolved by Large Eddy Simulations rather than a still thinner grid aspect ratio.

1 Introduction

The rapid expansion of offshore wind energy along the US East Coast has transformed the Southern New England (SNE) continental shelf into one of the most intensively developed offshore wind regions in the world. The lease areas south of Martha's Vineyard and Nantucket alone account for more than 13 GW of planned capacity as of May 2024 (McCoy et al., 2024), and the first commercial-scale project in the region, the 132 MW South Fork Wind Farm, has been fully commissioned since March 2024. However, this unprecedented scale of deployment raises fundamental scientific challenges regarding how massive wind plants interact with the complex dynamics of the atmosphere and ocean. As outlined in the grand challenges of wind energy (Veers et al., 2022), and specifically regarding the marine atmospheric boundary layer (Shaw et al., 2022), moving beyond basic resource assessment requires determining how accurately mesoscale atmospheric models can represent wake dynamics and air-sea interactions under the highly specific meteorological conditions that actually prevail over these lease areas.

The dominant marine atmospheric boundary layer (MABL) regime over the SNE shelf in spring and summer is persistently stable. Cold shelf water, isolated beneath the seasonal thermocline as the Mid-Atlantic Bight Cold Pool (Lentz, 2017), holds sea surface temperatures well below the temperature of continental air advected from the southwest. The resulting stable layer is shallow: over the Gulf of Maine, where the same advective contrast operates, its thermal structure is set by the near-constant difference between the water temperature and the continental air aloft rather than by fetch or by time of day, and the layer is only 50–100 m deep (Angevine et al., 2006). Direct-covariance flux measurements at the Martha's Vineyard Coastal Observatory show that stable surface-layer stratification is likewise the dominant state over the SNE shelf from May onward, peaking in midsummer (Chang and Kirincich, 2025). In this regime the turbulence dissipation rate offshore is roughly two orders of magnitude smaller than at comparable onshore sites, sustaining strong and long-lived wind farm wakes (Bodini et al., 2019), while suppressed vertical mixing enhances shear and veer across the rotor layer (Svensson and Holtslag, 2009; Holtslag et al., 2013). Beneath this stable atmosphere the upper ocean restratifies rapidly through spring: surface heating builds the seasonal

https://doi.org/10.5194/wes-2026-147
Preprint. Discussion started: 10 September 2026

eawe european academy of wind energy
Open Access WIND ENERGY SCIENCE DISCUSSIONS

thermocline and shoals the mixed layer from its deep, winter-mixed state to a climatological May depth of approximately 8 m over the SNE shelf (de Boyer Montégut, 2024). These conditions have direct consequences for the lease areas themselves: year-long simulations of the mid-Atlantic build-out find the strongest and longest wakes under summertime stable stratification, propagating tens of kilometers and coinciding with peak regional electricity demand (Rosencrans et al., 2024). Resolving this regime therefore requires a model that captures the vertical structure of a boundary layer that is shallower than the rotor layer it must also support.

García-Santiago et al. (2024) documented systematic stability-dependent differences in wind-farm parameterization performance benchmarked against high-resolution wake simulations, but the sensitivity of these simulations to vertical resolution has not been isolated from parameterization performance under stable marine conditions. This is a consequential gap, given the well-known difficulty NWP models face in resolving the sharp inversions that cap the stable boundary layer (Holtslag et al., 2013). The Fitch scheme is coupled here to MYNN2 (Nakanishi and Niino, 2004, 2009), the closure for which it was formulated. To evaluate the structural error inherent in boundary layer schemes like MYNN2, otherwise identical turbine-free simulations with the YSU scheme (Hong et al., 2006) are used to bracket how far the simulated structure of the stable MABL itself depends on closure choice, independent of any wind farm effect. Both are one-dimensional column closures that intended for shallow aspect ratio grid cells and so parameterize vertical fluxes alone and assume horizontal homogeneity within a grid cell. Rybchuk et al. (2022) showed that relaxing this assumption, by coupling Fitch to a three-dimensional PBL scheme, changes simulated wakes appreciably; that limitation is common to both schemes used here, and how far vertical refinement can usefully be pursued while it remains in place, at kilometer-scale grid spacing, is itself an open question.

A second major frontier in offshore wind modeling is the response of the upper ocean to wind farm forcing. By extracting momentum from the atmosphere, offshore wind farms reduce surface wind stress over large footprints; the resulting horizontal stress gradient adjusts the Ekman transport and generates a dipole in sea surface elevation, with corresponding anomalies in vertical velocity (Broström, 2008). North Sea studies have approached these effects from both directions. Hydrodynamic modeling reproduces the large-scale structures that emerge beneath atmospheric wind farm wakes (Christiansen et al., 2022), while towed-CTD surveys through operational wind farm wakes resolve the hydrographic fingerprint of the dipole changes in mixed layer depth and potential energy anomaly over distances below 5 km, and thermocline excursions of 10–14 m although the associated vertical velocity anomalies themselves remained below the detection limit of the survey (Floeter et al., 2022). Seo et al. (2025) extended this work to the US East Coast, showing with coupled simulations that large-scale lease-area build-out drives seasonal sea surface warming and mixed layer shoaling, and that the resulting upward heat flux destabilizes the MABL and enhances wind stress, partially offsetting the atmospheric wake. Such perturbations may also propagate into the ecosystem: Daewel et al. (2022) project changes in primary production and bottom-water oxygen under North Sea build-out scenarios.

Consequently, three specific knowledge gaps motivate this study: (1) the sensitivity of the Fitch-scheme atmospheric wake to vertical resolution under real-world stable marine ABL conditions has not been quantified, nor has the vertical resolution required for such simulations to be grid-converged been established; (2) the physical consequences of the PBLH falling below

https://doi.org/10.5194/wes-2026-147
Preprint. Discussion started: 10 September 2026

eawe european academy of wind energy
Open Access WIND ENERGY SCIENCE DISCUSSIONS

the turbine hub height have not been systematically evaluated in mesoscale wake modeling; and (3) the sensitivity of the mechanical ocean mixed layer (OML) response to atmospheric grid discretization is entirely unknown for the SNE lease area.

Here, we address these gaps through a suite of 15 WRF-Fitch-OML mesoscale simulations of a large offshore wind farm over the SNE Vineyard Wind lease area. Simulating a representative stable atmospheric episode in May 2018, we test five vertical atmospheric grid configurations, labeled by their first-layer thickness ($\Delta z = 5$–100 m) and spanning 27 to 2 model levels within the rotor swept zone, and two ABL schemes (MYNN2: Nakanishi and Niino 2004, 2009; YSU: Hong et al. 2006), coupling the atmospheric domain to a 1D ocean mixed layer (OML) model to diagnose the resulting air-sea coupling. Section 2 describes the data, model configuration, and validation. Section 3 presents results and discussion, detailing the background ABL structure, spatial wake characteristics, stability-dependent PBLH perturbations, and the ocean mixed layer response. Section 4 summarizes the main conclusions.

2 Data and Methods

2.1 Study region and ERA5 climatological context

The Southern New England (SNE) offshore wind lease area is situated approximately 15-25 nautical miles south of Martha's Vineyard and Nantucket, Massachusetts, over the Mid-Atlantic Bight continental shelf at water depths of 30-60 m. The region lies downstream of the Gulf Stream SST front, which in spring positions cold shelf waters (10-14 °C) of northern origin beneath warmer continental air masses advected from the southwest, establishing a persistently stable marine atmospheric boundary layer (MABL). This thermodynamic configuration, warm air overlying a cool ocean surface, suppresses convective mixing and maintains a shallow, stable ABL which is the primary regime of focus for this study.

Atmospheric stability is quantified throughout this study using the dimensionless stability parameter $\zeta = \frac{z}{L}$, where L is the Obukhov length (Monin and Obukhov, 1954):

$$L = -\frac{u_\star^3 \theta_v}{\kappa g \overline{w'\theta_v'}_s} \tag{1}$$

where $u_\star$ is the friction velocity, θ_v the virtual potential temperature, $\kappa = 0.4$ the von Karman constant, g the gravitational acceleration, and $\overline{w'\theta_v'}_s$ the surface buoyancy flux. Positive ζ indicates stable stratification corresponding to a downward buoyancy flux with an ocean surface cooler than the overlying air.

The persistence of this regime is documented through observations. Direct covariance flux measurements at the Air-Sea Interaction Tower (ASIT) of the Martha's Vineyard Coastal Observatory, 3.2 km south of Martha's Vineyard in 15 m of water and approximately 40 km north of the lease area, provide a 16-year record of surface-layer stability over the same shelf (Chang and Kirincich, 2025). The observed climatology (Fig. 1) shows that the air-sea temperature difference over the inner shelf reverses sign in spring: $T_{air} - T_{sea}$ is negative through winter, crosses zero in May, and remains positive through the summer. Stable stratification ($0 < L < 200$ m, equivalent to $\zeta_{10} > 0.05$) is the dominant surface-layer state from May onward, and the

https://doi.org/10.5194/wes-2026-147
Preprint. Discussion started: 10 September 2026

observations confirm that the warm air over cool water configuration described above is a persistent feature of this shelf rather than a model artifact. May marks the onset of this regime and carries the largest interannual spread of the stable season.

To identify the month in which this regime coincides with turbine-relevant wind conditions, we analyzed ERA5 reanalysis data (Hersbach et al., 2020) at 0.25° horizontal resolution and 1-hourly temporal resolution over the SNE lease area for the period 2015-2024. Hourly ERA5 PBLH, 10-m wind speed and Obukhov length were extracted over the lease area domain (Fig. 2) and averaged to daily means. We define a shallow stable event as a day whose daily means satisfy three simultaneous criteria: PBLH $\leq$ 300 m, stability parameter $\zeta = \frac{z}{L} > 0.05$ evaluated at $z = 10$ m, and hub-height wind speed U_{hub} in the operational range 8-16 $\mathrm{m\,s^{-1}}$. Daily averaging is used throughout the selection because the simulation window is itself chosen to have a multi-day duration. Applied individually, the criteria are nearly degenerate between May and June: shallow boundary layers occur on 49.7% of May days against 48.0% of June days, and stable stratification on 55.8% against 54.0%, while June in fact registers the lower monthly mean PBLH (347 m against 365 m). The joint criterion separates the two decisively, with shallow stable events on 15.8% of May days against 7.0% in June, 8.0% in April and 2.3% in July (Fig. 3a). The discriminating constraint is the operational wind range, which is satisfied on 55.8% of May days but only 46.7% of June days and 33.2% of July days, so the months of strongest stratification coincide with the seasonal wind minimum. May was therefore selected as the target month, as the month in which shallow stable conditions and turbine-relevant winds co-occur most often. Note that a different month is most strongly stratified: the observations show stratification continuing to strengthen into midsummer (Fig. 1), when the seasonal wind minimum occurs. These findings are consistent with observations of the highly stable MABL over the Gulf of Maine (Angevine et al., 2006).

https://doi.org/10.5194/wes-2026-147
Preprint. Discussion started: 10 September 2026

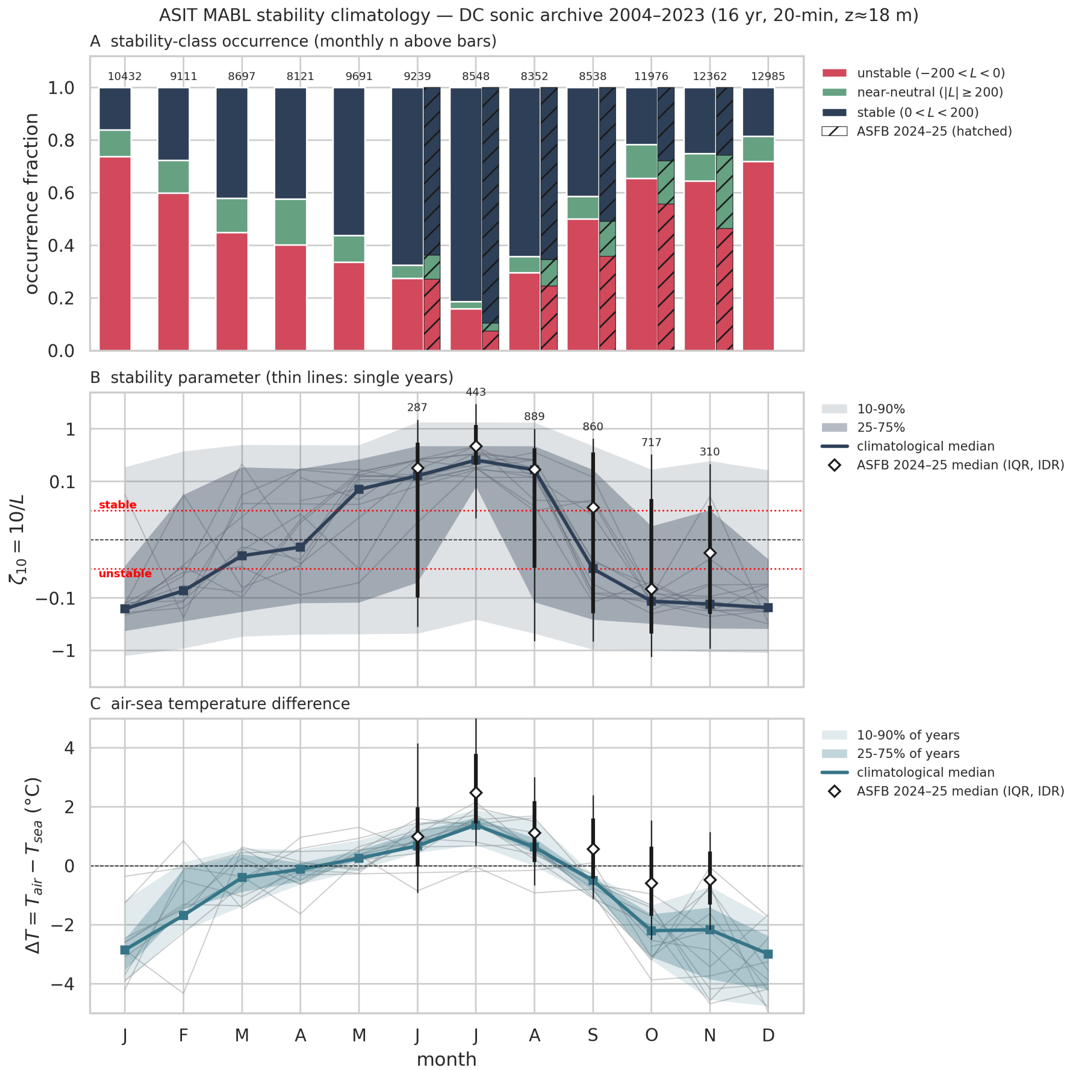

Figure 1. Observed climatology of marine atmospheric surface-layer stability over the New England shelf, from direct covariance flux measurements. (a) Monthly occurrence of stability classes at the Martha's Vineyard Coastal Observatory Air-Sea Interaction Tower (ASIT; 41°19.5′N, 70°34.0′W, $z \approx 18$ m), from 20-minute flux estimates spanning 16 years within the period 2004-2023 (Chang and Kirincich, 2025). Classes follow the Obukhov length: unstable ($-200 < L < 0$ m), near-neutral ($|L| \geq 200$ m) and stable ($0 < L < 200$ m), equivalent to $\zeta_{10} = 10/L$ below -0.05, within ± 0.05, and above $+0.05$ respectively; sample counts are annotated above each bar. Hatched bars show the corresponding occurrence from the University of New Hampshire air-sea flux buoy (ASFB) deployed off the New Hampshire coast during 2024-25 (Laxague et al., 2026). (b) Monthly distribution of the stability parameter $\zeta_{10} = 10/L$ at ASIT: climatological median (solid), interquartile and 10-90% ranges (shading), and individual years (thin grey); diamonds and bars give the ASFB median, interquartile and interdecile ranges. Red dotted lines mark the ± 0.05 class boundaries. (c) As (b), for the air-sea temperature difference $\Delta T = T_{air} - T_{sea}$. The two sites lie in different basins but show the same seasonal structure: ΔT reverses sign in spring, and stable stratification dominates the surface layer from May through the summer, peaking in midsummer. The seasonal maximum in stratification is not coincident with the regime targeted here, which additionally requires hub-height winds within the turbine operating range. (Data collected by N. Laxague.)

https://doi.org/10.5194/wes-2026-147
Preprint. Discussion started: 10 September 2026

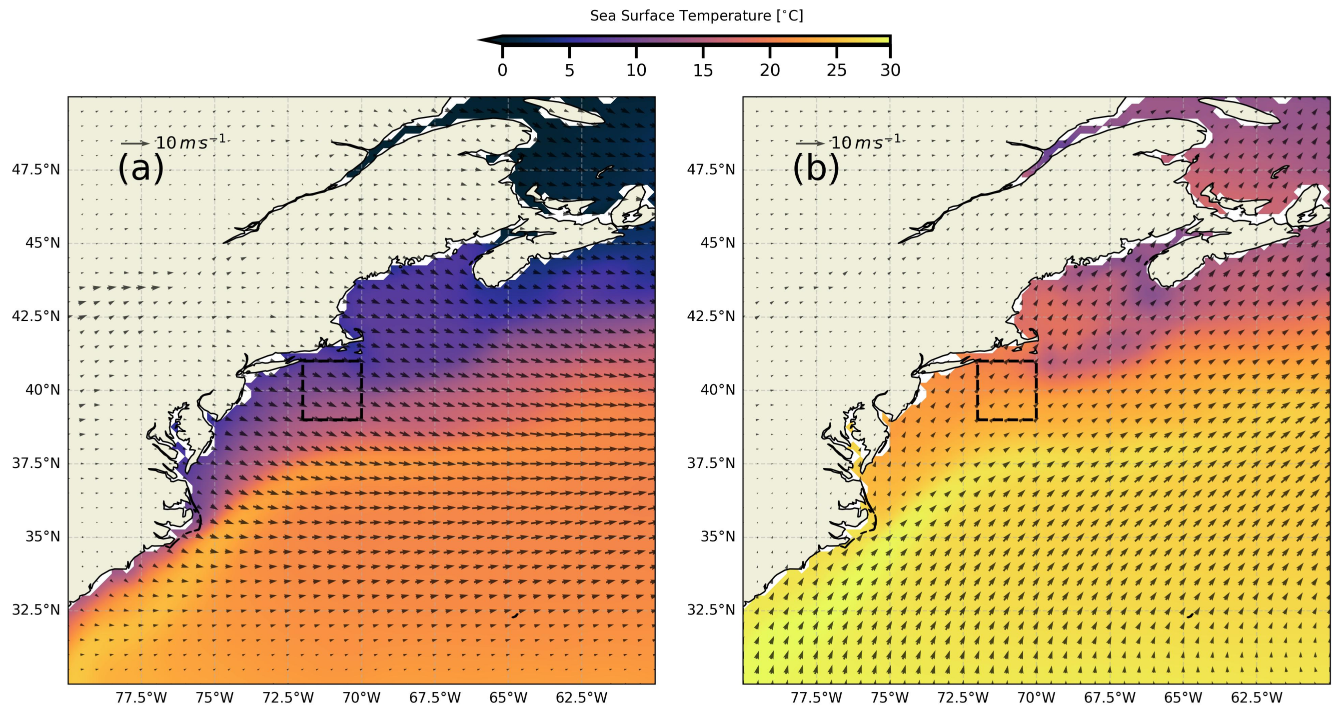

Figure 2. ERA5 sea surface temperature (SST, °C) and 10-m wind vectors over the western North Atlantic during (a) winter and (b) summer. The box indicates the SNE lease area.

2.2 Simulation window selection

Based on this climatology, we selected the period 2-8 May 2018 as the simulation window. Candidate seven-day windows were ranked by a composite score combining the fraction of qualifying days, the window-mean PBLH relative to the 300 m threshold, and the window-mean stability. Of 3648 candidate windows in the 2015-2024 record, none contained six or more qualifying days, exactly one contained five, and sixteen contained four or more. Sustained multi-day occurrences of the joint regime are therefore rare, and 2-8 May 2018 is the strongest realization available in the record rather than a typical week: at 235 m it has the lowest May mean PBLH of the ten Mays analyzed, and its qualifying-day fraction of 35% lies in the 90th percentile of that distribution. May is also the most interannually variable month of the stable season in the reanalysis, with mean z/L ranging from -0.002 to $+0.166$ across the record, consistent with the observed spread (Fig. 1). Selecting a strongly expressed episode is deliberate for a sensitivity study, in which a clear signal is required to separate resolution effects from noise, but the window should not be read as climatologically representative.

This period satisfies the three qualifying criteria on five of seven days (Fig. 3b), with a period mean PBLH of 263 m and a mean hub-height wind speed of 11 $\mathrm{m\,s^{-1}}$. The criteria serve to select the window; the full seven-day period is simulated and retained in all subsequent analysis, and no days are discarded. The daily-mean threshold $\zeta > 0.05$ used here to select the

https://doi.org/10.5194/wes-2026-147
Preprint. Discussion started: 10 September 2026

window is likewise distinct from the hourly threshold $z/L > 0.1$ used in Sect. 3 to composite stable conditions: the former identifies candidate periods, the latter isolates stable hours within the simulated window. The two days that do not meet the selection criteria illustrate the same trade-off that operates seasonally: 4 May exceeds the boundary-layer depth threshold (daily mean 331 m), while 7 May is the most strongly stratified day of the window ($z/L = 0.29$) but has a daily mean hub-height wind speed of 6.8 m s^{-1}, below the operational range. Retaining both is deliberate, as they broaden the range of conditions sampled and contribute to the stability bins examined in Sect. 3.3. The flow is predominantly southwesterly: the southwest sector (191–259°) accounts for 50% of hours over the analysis period (Fig. 4b), and the lease-area-mean stability exceeds $z/L = 0.1$ for 80% of hours, with a median of 0.18, so the window is stable for the large majority of its duration. This directional persistence is consistent with the ERA5 climatological mean for May over the lease area and ensures that the along-wind transect analysis presented in Section 3 captures the primary wake propagation direction. The window spans seven diurnal cycles, over which the lease-area PBLH varies by approximately 75 m, shallowest near midday and deepest near 04:00 local time; this is sufficient to characterize the diurnal response, although the window samples a single synoptic regime and the results should not be read as spanning synoptic variability.

All WRF simulations are initialized at 00:00 UTC on 1 May 2018, and the first 24 hours are discarded as spin-up: every quantity reported below is computed over the 168 hourly outputs from 00:00 UTC 2 May to 23:00 UTC 8 May, including the profiles, the scalar diagnostics, the difference maps and the transects. Two further conventions apply throughout Sect. 3. Lease-area means over stable conditions are point-hour weighted, so that every stable grid-point-hour carries equal weight and hours in which a larger fraction of the lease area is stable contribute proportionally more; averaging the hourly spatial means with equal weight instead changes the reported lease-area mean PBLH by 7% and the other scalars by 2–5%. Stability is always classified from the no-farm run at each grid point and hour, for both members of a wind-farm/no-farm pair, so that the two runs are averaged over an identical set of point-hours and the difference of the time-mean fields is exactly the time-mean of the differences.

https://doi.org/10.5194/wes-2026-147
Preprint. Discussion started: 10 September 2026

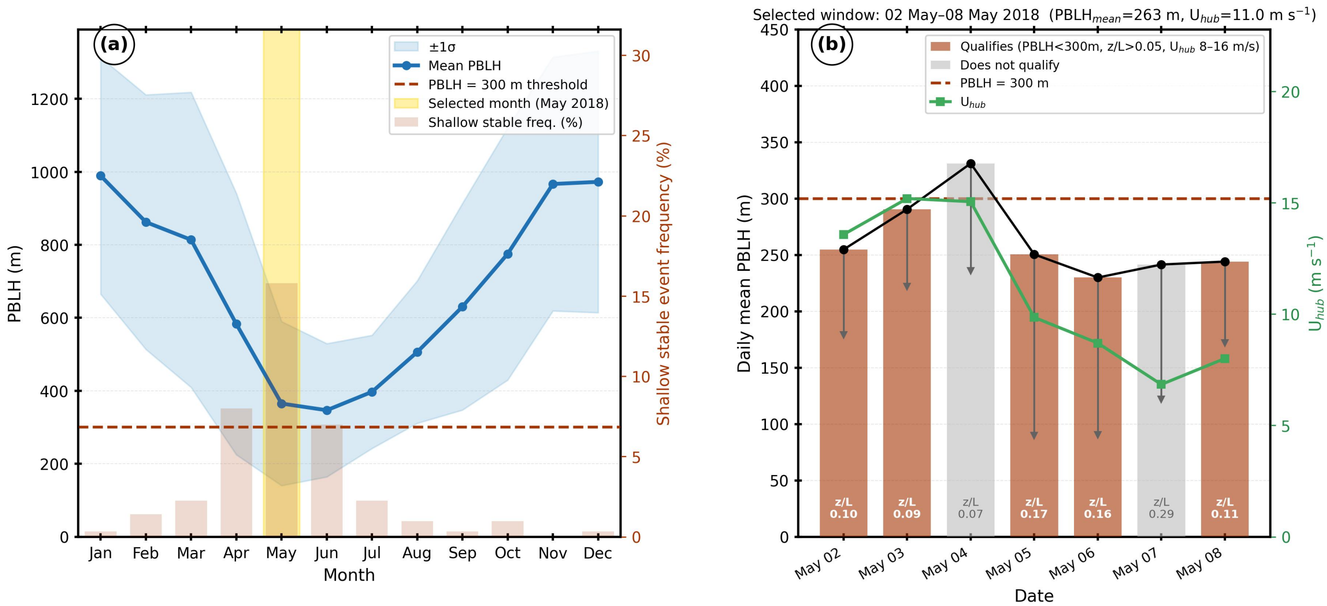

Figure 3. (a) ERA5 monthly mean planetary boundary layer height (PBLH, m, left axis; blue line $\pm$ 1σ) and the frequency of shallow stable event days (PBLH $\leq$ 300 m, $z/L > 0.05$, U_{hub} = 8-16 m s^{-1}; right axis; pink bars) over the SNE lease area for 2015-2024, both evaluated on daily means. The dashed red line marks the 300 m threshold. May maximizes the joint criterion (yellow shading), motivating its selection as the simulation month; the individual criteria are near-degenerate between May and June, and mean PBLH is lowest in June. (b) Daily mean PBLH (black line), U_{hub} (green line, right axis), and mean z/L (annotated bars) for 2-8 May 2018. Orange bars: days satisfying all qualifying criteria; grey bars: days not meeting the criteria, which are nonetheless simulated and retained in the analysis.

2.3 WRF model configuration

Atmospheric simulations were conducted using the Weather Research and Forecasting model (WRF-ARW version 4.4: Skamarock et al., 2019), following the modeling framework of Seo et al. (2025) for the US East Coast offshore wind context. Two one-way nested domains were configured: an outer domain (d01) at 7.5 km horizontal grid spacing covering the broader northwest Atlantic, and an inner domain (d02) at 1.5 km horizontal grid spacing centered on the SNE lease areas (Fig. 4a). Both domains use an integration time step of 20 s on d01, with a parent time-step ratio of 5.

Near-surface vertical resolution is the primary sensitivity parameter of this study. Five configurations were tested, labeled by their first-layer thickness, Δz = 5, 10, 25, 50 and 100 m. The vertical grid stretches continuously with height in every configuration, so Δz is a label for the near-surface refinement rather than a spacing held uniform over any fixed depth. Table 1 gives the resulting geometry, measured from the model geopotential rather than from the namelist. The mean layer thickness over the lowest 250 m, which spans the rotor, is 7, 11, 26, 47 and 79 m respectively, and the number of model levels within the rotor swept zone falls from 27 to 2 across the ensemble, a range of 13.5:1. At Δz = 100 m the lowest mass level lies at 50 m, above the rotor bottom tip, so that configuration carries no information in the lower part of the rotor. Above the near-surface

https://doi.org/10.5194/wes-2026-147
Preprint. Discussion started: 10 September 2026

Table 1. Vertical grid geometry of the five configurations, measured from the model geopotential over the lease area. Δz labels the first-layer thickness; the grid stretches continuously above it. The rotor swept zone spans 30–246 m and the hub is at 138 m. Values are identical for the MYNN2 and YSU configurations, which share the same vertical levels.

Δz label (m)	first layer (m)	lowest mass level (m)	mean thickness below 250 m (m)	levels in rotor	levels below hub	total levels
5	2.5	1.2	7.4	27	24	92
10	5.0	2.5	11.3	18	13	80
25	12.5	6.2	26.4	8	5	60
50	25.0	12.5	47.4	3	3	49
100	50.1	25.0	78.8	2	1	40

region the grid stretches toward the domain top at approximately 50 hPa, and the five configurations use 92, 80, 60, 49 and 40 vertical levels in total.

The five configurations were chosen to span, in approximately geometric steps, the range of near-surface vertical resolutions encountered in practice. The finest, $\Delta z = 5$ m, resolves the rotor layer with 27 model levels and serves as the reference against which the others are compared; the coarsest, $\Delta z = 100$ m, places only two levels within the rotor and its lowest level above the bottom tip, a configuration representative of the near-surface grids used by operational regional forecast models, which are not designed to resolve a rotor layer. The intermediate values fill the range so that the ensemble samples the transition between the two regimes rather than only its endpoints. The $\Delta z = 5$ m configuration is used as the reference throughout the paper. Its adequacy as a reference is assessed in Sect. 3.1.

The near-surface grid is constrained by the vertical Courant condition on the outer domain. With a 20 s time step at 7.5 km horizontal spacing, layer thicknesses below roughly 15 m at the top of the rotor produce vertical Courant numbers above unity in convective cells over land in the far corners of d01, well outside the lease area but sufficient to terminate the integration. The stretching in each configuration is therefore set so that the layer thickness reaches at least 15 m by 250 m, matching the envelope of the vertical grid used by Seo et al. (2025) over the same domain at the same time step. This is a concrete instance of the aspect-ratio constraint that arises when meter-scale vertical resolution is combined with kilometer-scale horizontal resolution: the achievable near-surface refinement is limited by the outer domain rather than by the inner domain where the resolution is wanted.

Initial and lateral boundary conditions were derived from ERA5 reanalysis data at 0.25° resolution and 1-hourly temporal resolution (Hersbach et al., 2020). The model physics suite was held the same across all simulations. Longwave and shortwave radiation were parameterized using the Rapid Radiative Transfer Model for GCMs (RRTMG: Iacono et al., 2008). Cloud microphysics followed the Thompson et al. (2008) graupel scheme. Land surface processes were represented by the Noah Land Surface Model (Chen and Dudhia, 2001).

https://doi.org/10.5194/wes-2026-147
Preprint. Discussion started: 10 September 2026

eawe european academy of wind energy
Open Access WIND ENERGY SCIENCE DISCUSSIONS

Surface fluxes and ocean skin temperature over the ocean were computed using the Pollard-Rhines-Thompson (PRT) 1D ocean mixed layer model (Pollard et al., 1973) as implemented in WRF, which prognostically updates both the mixed-layer temperature (which sets the ocean skin temperature, TSK, that is seen by the atmosphere) and the mixed layer depth (H_{ml}) as a function of wind-driven mechanical stirring and surface buoyancy flux. The initial mixed layer depth was set to 8 m, the May climatological mixed layer depth over the Southern New England shelf from global climatology (de Boyer Montégut, 2024). The deep water temperature lapse rate was set to $\gamma = 0.02\ \mathrm{K\ m^{-1}}$, computed as the maximum local lapse rate $\max(-\partial T/\partial z)$ in the stratified deep water below the $\sim 100\ \mathrm{m}$ of the HYCOM GOFS 3.1 May 2018 temperature profile at the SNE lease centroid. Through this coupling, the wind-farm-induced reduction in surface stress weakens the mechanical stirring of the ocean mixed layer, which in turn shoals the mixed-layer depth, reducing entrainment and raising mixed layer and skin temperatures; this is the air-sea feedback diagnosed in Section 3.4.

Two planetary boundary layer (ABL) schemes were evaluated: the Mellor-Yamada-Nakanishi-Niino level-2.5 scheme (MYNN2: Nakanishi and Niino, 2004, 2009) and the Yonsei University scheme (YSU: Hong et al., 2006). Both are among the most widely used schemes in offshore wind applications and were the pair identified by Rybchuk et al. (2022) as a primary source of wake uncertainty in US offshore simulations, which is why they are the two examined here. MYNN2 employs a prognostic TKE equation with stability-dependent mixing length closure, making it well-suited for stable stratification. YSU uses a non-local K-profile approach with an explicit entrainment flux term. MYNN2 is used as the primary reference throughout the paper; YSU noWF results are presented alongside for comparison in the background ABL characterization (Section 3.1). Wind farm simulations (WF) were conducted only with MYNN2, as it is the recommended ABL scheme for use with the Fitch parameterization under stable marine conditions (Rybchuk et al., 2022; García-Santiago et al., 2024). This yields a total of 15 simulations (10 without wind farms and 5 with wind farms).

2.3.1 Wind farm parameterization

Wind turbine effects were represented using the Fitch wind farm parameterization (Fitch et al., 2012, 2013) as implemented in WRF-ARW. The Fitch scheme represents each turbine as a momentum sink and TKE source distributed across model levels intersecting the rotor disk. The thrust and power coefficients are prescribed as functions of hub-height wind speed, and the momentum extracted at each level is proportional to the fraction of rotor area contained within that level. The turbine-induced TKE source term uses the correction factor $\alpha = 0.25$ proposed by Archer et al. (2020) to address the overestimation of TKE generation identified in the original Fitch formulation through comparison with large-eddy simulations.

Turbine specifications follow the 12 MW turbine configuration of Seo et al. (2025), with a rotor diameter of $D = 215$ m and a hub height of $H_{hub} = 138$ m, placing the rotor swept zone between 30 (bottom tip) and 246 m (top tip) above the surface. The turbine layout and SNE lease area configuration also follow Seo et al. (2025). Because the Fitch scheme distributes the momentum sink over the model levels intersecting the rotor disk, the number of levels within that zone (Table 1) sets the vertical structure the parameterization can represent, and is the mechanism by which vertical resolution enters the wake calculation.

2.4 Model validation

Model performance was evaluated against hourly observations from two NDBC buoys (44017 and 44025) over the analysis period (165 and 166 matched hours respectively, after the spin-up day is excluded). Model wind speed was interpolated to each buoy's anemometer height (4.1 m at 44017, 5.0 m at 44025) by linear interpolation between the two lowest model levels, and assessed together with 2 m air temperature (ATMP) at both buoys on a normalized Taylor diagram (Taylor, 2001) for the MYNN2 and YSU ($\Delta z = 5$ m) noWF simulations (Fig. 4c).

Both schemes reproduce the wind speed variability well, with normalized standard deviations of 0.86–1.00, correlations of 0.76–0.83 and RMSE of 1.6–1.8 $\mathrm{m\,s^{-1}}$. MYNN2 carries the larger wind-speed RMSE at both buoys (1.76 and 1.79 $\mathrm{m\,s^{-1}}$, against 1.61 for YSU), reflecting primarily a positive near-surface wind bias, but also the normalized standard deviation closest to unity (0.93 and 1.00, against 0.86 and 0.87), so YSU underestimates the amplitude of the observed variability while MYNN2 reproduces it. Air temperature is less well captured: normalized standard deviations of 0.51–0.76, correlations of 0.50–0.64 and RMSE of 0.9–1.1 °C, with centred RMS errors of 0.78–0.87 comparable to the observed standard deviation. This is expected over a seven-day window within a single synoptic regime, in which the observed 2 m temperature varies over a narrow range so that the correlation is computed against limited signal, and it should not be read as a characterization of the model's temperature skill over longer periods. The validation establishes that the simulated near-surface wind field, the quantity on which the wake analysis depends, is realistic; it does not extend further.

https://doi.org/10.5194/wes-2026-147
Preprint. Discussion started: 10 September 2026

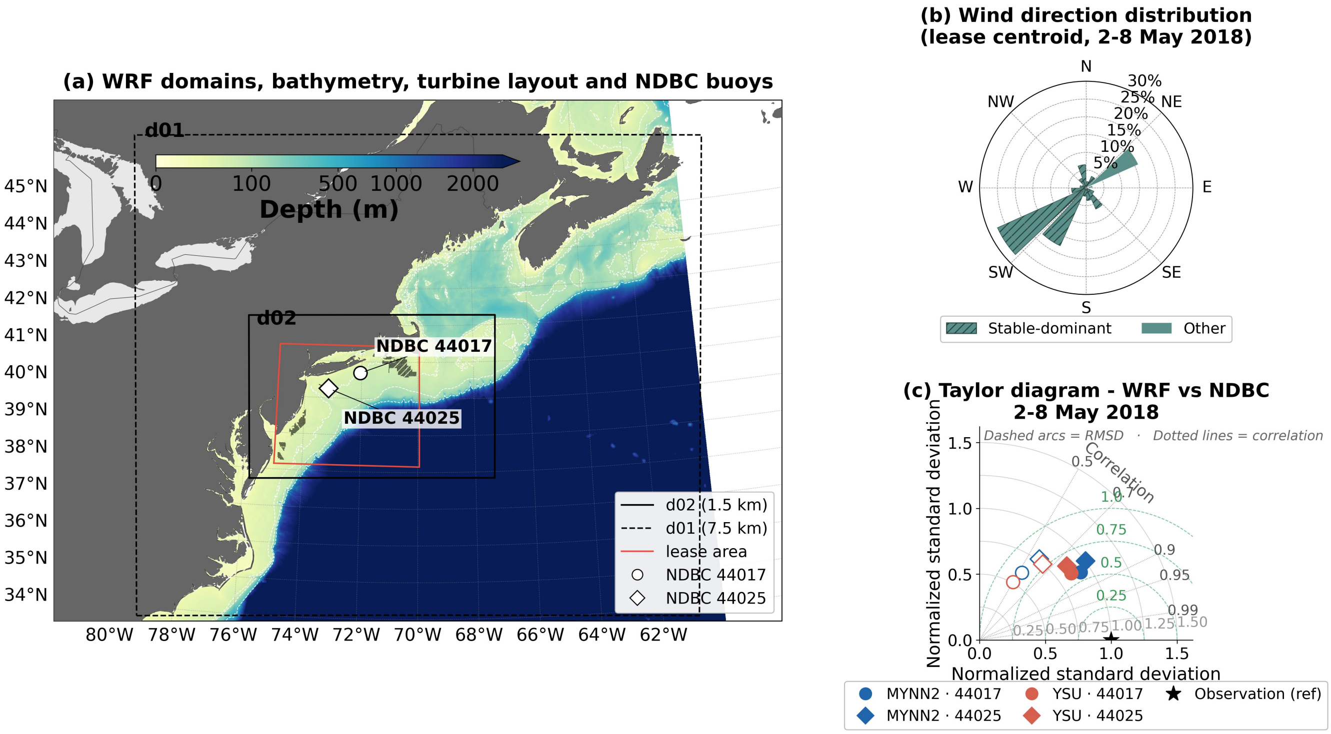

Figure 4. Model configuration and validation. (a) WRF nested domains, d01 (dashed black outline, 7.5 km) and d02 (solid black, 1.5 km), with bathymetry (shading, white dashed depth contours at 50, 100 and 500 m), the turbine layout (black dots) and the modeled lease areas across the Southern New England (SNE) Bight; the red box marks the lease-area analysis domain. The two NDBC buoys used for validation are shown as white markers, 44017 as a circle and 44025 as a diamond. (b) Distribution of the lease-area-mean 10 m wind direction over the analysis period (2–8 May 2018); bars are hatched where the lease-area-mean stability exceeds $z/L = 0.1$. (c) Taylor diagram comparing simulated and NDBC-observed near-surface fields for the Δz = 5 m configurations. Colour denotes the ABL scheme (blue MYNN2, red YSU) and marker shape the buoy, using the same shapes as in (a); filled markers are wind speed at the anemometer height (4.1 m at 44017, 5.0 m at 44025) and open markers are 2 m air temperature. The black star is the observation reference (normalized standard deviation 1, correlation 1); radial distance from the origin is the normalized standard deviation, azimuth is the correlation, and distance from the star is the centered RMS error.

https://doi.org/10.5194/wes-2026-147
Preprint. Discussion started: 10 September 2026

3 Results and Discussion

3.1 Stable marine atmospheric boundary layer structure

The time-mean vertical profiles of wind speed and potential temperature over the SNE lease area during stable events ($\frac{z}{L} > 0.1$) are shown in Fig. 5. Both ABL schemes produce a strongly sheared wind profile through the lower rotor layer, rising from 8.9 $\mathrm{m\,s^{-1}}$ (MYNN2) and 7.7 $\mathrm{m\,s^{-1}}$ (YSU) at the rotor bottom tip to 12.4 and 12.3 $\mathrm{m\,s^{-1}}$ at hub height, and remaining near 12.4 $\mathrm{m\,s^{-1}}$ at the rotor top in both schemes. Almost all of the shear across the rotor is therefore concentrated below hub height: of the 3.5 $\mathrm{m\,s^{-1}}$ (MYNN2) and 4.8 $\mathrm{m\,s^{-1}}$ (YSU) increase between the bottom and top tips, the wind speed is essentially constant over the upper half of the disk. This is accompanied by a sharp potential temperature inversion concentrated in the lowest 100 m, rising by 6.7 K (MYNN2) and 7.2 K (YSU) between the bottom and top tips. This structure is characteristic of the stable marine internal boundary layer that forms when warm continental air is advected over cooler shelf waters, documented over the Gulf of Maine (Angevine et al., 2006) and over the Mid-Atlantic Bight (Jiang and Edson, 2021), a stable cool-water regime shown to enhance vertical shear and hub-height winds with direct consequences for offshore wind energy (Pareja-Roman et al., 2024).

This bottom-weighted shear structure is qualitatively consistent with lidar observations at Block Island, some 60 km west of the lease area, collected during the WFIP3 campaign (Wind Forecast Improvement Project 3, 2025). Under stable conditions in May the observed power-law exponent over the rotor span is 0.20–0.22 across hub-height wind speeds of 9–15 $\mathrm{m\,s^{-1}}$, and 0.21 in the bin bracketing the simulated hub-height wind speed. The simulated exponents are of the same order, with YSU (0.20) close to the observed value and MYNN2 (0.13) roughly a factor of 1.5 lower. The comparison is qualitative: the observational record does not overlap the simulated week, and the exponent is sensitive to the layer over which it is evaluated, falling from 0.28 between the bottom tip and hub height to 0.08 between hub height and the rotor top.

The two ABL schemes agree on the shape of these profiles but disagree substantially on the boundary layer height (PBLH): MYNN2 diagnoses 118 m and YSU 92 m, a 29% difference. Both lie well below hub height, so that 59% (MYNN2) and 72% (YSU) of the rotor swept area sits above the boundary-layer top. This difference reflects their distinct stable turbulence parameterizations. MYNN2 sustains mixing to greater heights through a prognostic TKE equation that explicitly represents the production, transport, and dissipation of turbulent kinetic energy under stable stratification (Nakanishi and Niino, 2009). YSU applies a bulk Richardson number criterion that produces a more abruptly capped stable layer (Hong et al., 2006). The consequences of this choice are well documented and regionally contingent. Bodini et al. (2024) selected the best-performing WRF configuration for each US offshore region from a 16-member ensemble validated against floating lidars, and found that MYNN performed best over the North and Mid-Atlantic while YSU was preferred in the South Atlantic, Gulf of Mexico and South Pacific. Off the northern California coast, Liu et al. (2024) attributed the majority of the modelled wind bias to the PBL scheme, with MYNN overestimating the frequency of stable conditions and producing larger warm-season hub-height errors than YSU. That the preferred scheme differs between regions, and that the two schemes here diverge by 29% in diagnosed PBLH under identical forcing, indicates that scheme choice remains a leading source of uncertainty in stable offshore conditions.

https://doi.org/10.5194/wes-2026-147
Preprint. Discussion started: 10 September 2026

The two variables respond very differently to vertical resolution. Potential temperature profiles are nearly indistinguishable across the four finest grids throughout the rotor swept zone for both schemes (Fig. 5b, d); the maximum departure from the reference inside the rotor is below 0.21 K for $\Delta z \leq 25$ m in MYNN2, rising to 0.60 K only at Δz = 100 m. The thermal stratification defining the stable regime is therefore robustly represented across the practical range of resolutions. Wind speed profiles are not (Fig. 5a, c), and the two schemes degrade in physically distinct places. In MYNN2 the maximum departure from the reference occurs at 38 m and 33 m for Δz = 25 and 50 m, near the rotor bottom tip, and reaches 0.63 m s^{-1} at Δz = 50 m; only at Δz = 100 m does the largest error move to 102 m, close to the boundary-layer top. In YSU the maximum departure lies between 102 and 148 m at every coarse resolution, that is, near the boundary-layer top throughout. MYNN2 therefore loses accuracy first in the lower rotor, where the shear is concentrated, while YSU loses it first near the inversion.

Part of this sensitivity is structural rather than parametric. The rotor swept zone spans 30–246 m and is sampled by 27 model levels at $\Delta z = 5$ m, 18 at 10 m, 8 at 25 m, 3 at 50 m and 2 at 100 m; the corresponding counts below hub height are 24, 13, 5, 3 and 1 (Table 1). At Δz = 100 m the lowest mass level lies at 50 m, above the rotor bottom tip, so the lower rotor is unsampled by construction and the near-surface shear cannot be represented there irrespective of the turbulence closure applied.

Figure 6 shows the resolution sensitivity compared to the $\Delta z = 5$ m reference. The friction velocity $u_\star$ is by far the most stable diagnostic, remaining within ±3.2% of the reference across the full range in both schemes and within ±1% in MYNN2. This reflects that the bulk surface-layer flux formulations are relatively insensitive to vertical discretization. Hub-height wind speed U_{hub} is similarly stable for $\Delta z \leq 50$ m in both schemes, departing by less than 1.2% in MYNN2 and 4.3% in YSU, but at Δz = 100 m it falls to −9.0% (MYNN2) and −6.7% (YSU), outside the ±5% band. The temperature scale $\theta^\star$ behaves differently between schemes: MYNN2 stays within 1.7% until Δz = 50 m before rising to +11.8% at 100 m, while YSU increases steadily from Δz = 25 m onward, reaching +19.7% at the coarsest resolution.

PBLH is the most sensitive diagnostic. Both schemes agree closely at Δz = 10 m, where the bias is below 4%, but diverge strongly beyond that point. The MYNN2 bias accelerates far more rapidly than YSU, reaching +15% at Δz = 25 m, +36% at 50 m and +87% at 100 m, where the diagnosed boundary layer is 222 m against 118 m in the reference. YSU diverges more moderately and saturates, reaching +11%, +19% and +22% at the same resolutions. These discrepancies occur because the temperature inversion defining the stable PBLH is sharp and concentrated over a height that is often shallower than a single layer at coarse resolutions. When vertical levels cannot resolve the inversion, the diagnosed boundary layer height is systematically overestimated, consistent with the difficulty of representing the stable boundary layer and its tendency toward excessive mixing in coarse models (Holtslag et al., 2013; Svensson and Holtslag, 2009).

The MYNN2 scheme is particularly sensitive because its prognostic TKE equation responds to the artificially smoothed inversion by sustaining spurious mixing to excessive heights, consistent with the general tendency of stable boundary layer schemes toward excessive mixing (Holtslag et al., 2013) and with the over-deepening reported for an offshore low-level jet case by Hawbecker et al. (2026).

The wind shear exponent α reveals the most significant contrast between the two schemes. Over the rotor layer, YSU degrades monotonically, reaching −3%, −8%, −19% and −42% as the grid is coarsened. MYNN2 does not: the bias is +0.6% at Δz = 10 m and −3.7% at 25 m, jumps to +23.0% at 50 m, and returns to −18.1% at 100 m. The 50 m spike is the

https://doi.org/10.5194/wes-2026-147
Preprint. Discussion started: 10 September 2026

feature that most obviously departs from a smooth trend, and its origin can be located. That configuration places its lowest three mass levels at 25, 76 and 131 m, so the wind speed at the 30.5 m bottom tip is obtained by interpolating across the 25–76 m layer, which is precisely the height range over which most of the rotor shear occurs; no model level lies within it. It is also the resolution at which the maximum profile departure from the reference sits lowest in the rotor, at 33 m. The α anomaly is therefore a lower-rotor sampling effect, distinct in origin from the boundary-layer-top error that drives the PBLH bias.

This interpretation is supported by evaluating α over a layer that every configuration resolves. Between 60 and 245.5 m, the YSU exponent is flat to within 1.5% out to Δz = 50 m and departs only at 100 m (-21%), so its apparent monotonic degradation over the rotor layer is almost entirely a lower-rotor effect. The MYNN2 spike at Δz = 50 m persists in the restricted layer ($+21\%$), confirming that it is not an artefact of the bottom-tip interpolation alone. At Δz = 100 m the rotor-layer exponent is evaluated between 52 and 245.5 m rather than the full rotor span, because the lowest model level lies above the bottom tip, and that value is therefore not strictly comparable to the others.

The adequacy of the $\Delta z = 5$ m reference can be assessed from the ensemble itself (Figs. 5–6). Differences between successive grids contract sharply toward the fine end for most diagnostics: between $\Delta z = 5$ and 10 m the MYNN2 hub-height wind speed differs by 0.09%, the friction velocity by 0.06% and the shear exponent by 0.6%, against 7.9%, 1.1% and 33% respectively between the two coarsest grids. Richardson extrapolation over the three finest grids, using the mean layer thickness below 250 m as the effective spacing, places the finest solution within 0.5% of the zero-spacing limit for $\theta_\star$ and, for YSU, within 0.1% for $u_\star$, 2.9% for U_{hub} and 3.9% for α. For the MYNN2 wind diagnostics the successive differences at the fine end are too small for the extrapolation to be well posed, which is itself evidence that those quantities have ceased to change. Thus $\theta_\star$, $u_\star$, U_{hub}, and α are effectively grid-converged in MYNN2 at the $\Delta z = 5$ m reference resolution (Fig. 6).

PBLH is the exception (Fig. 6a). It converges monotonically in both schemes but slowly, with an observed order of 0.71 (MYNN2) and 0.76 (YSU), and the finest solution lies 11.5% and 11.6% from the extrapolated limit, corresponding to a grid convergence index of about 13%. This reflects the nature of the diagnostic: the boundary-layer height is located by a threshold criterion evaluated on model levels, so its discretisation error is set by level placement rather than by the accuracy of an interpolated profile. The extrapolated limits, 106 m for MYNN2 and 82 m for YSU, are shallower than the simulated values, which would place a still larger fraction of the rotor above the boundary-layer top than reported above. Resolution-induced PBLH differences smaller than roughly 13% should therefore not be read as physical; the biases reported here, which reach 87% at the coarsest grid, exceed that bound by nearly an order of magnitude.

https://doi.org/10.5194/wes-2026-147
Preprint. Discussion started: 10 September 2026

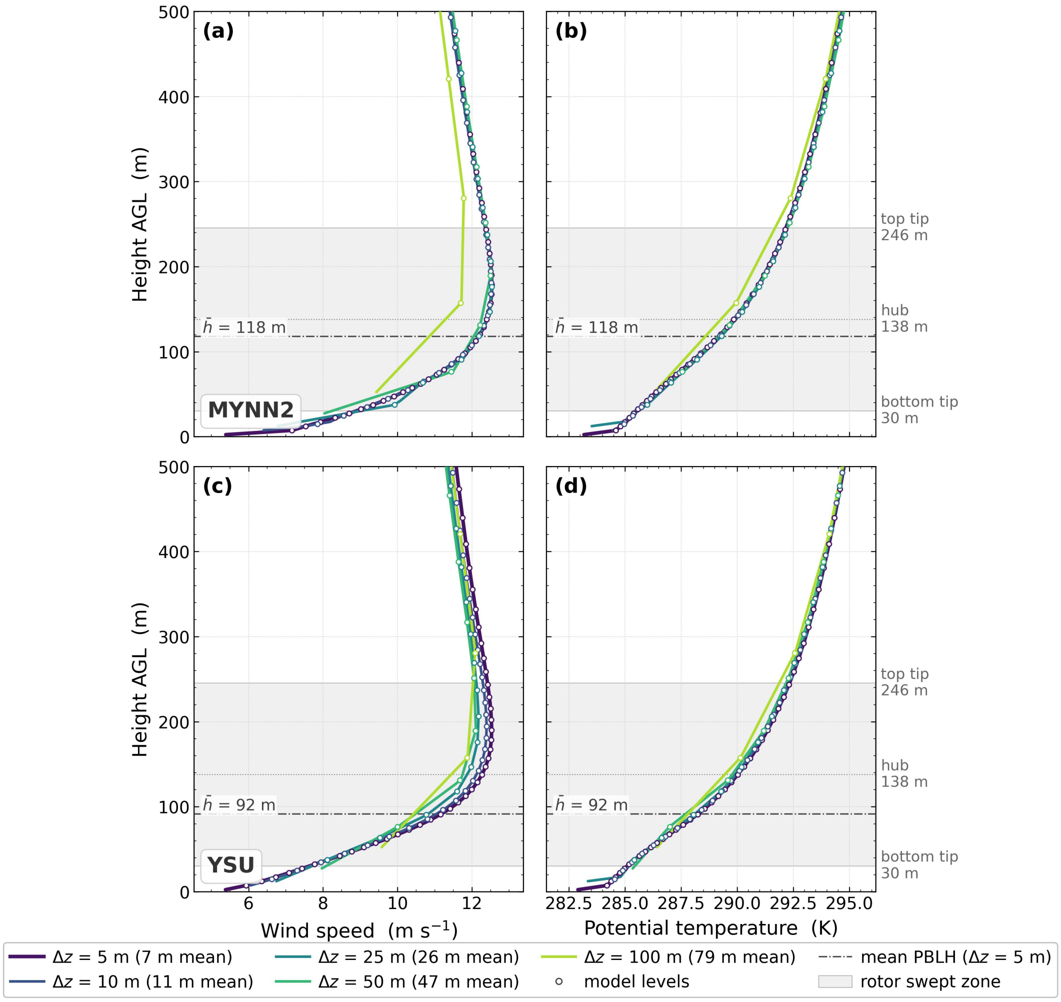

Figure 5. Vertical structure of the no-farm stable marine boundary layer and its sensitivity to vertical resolution. (a, c) Horizontal wind speed and (b, d) potential temperature, averaged over stable hours ($z/L > 0.1$) during 2–8 May 2018, for (a, b) the MYNN2 scheme and (c, d) the YSU scheme. Colours denote the five vertical configurations, labeled by their first-layer thickness (Δz = 5, 10, 25, 50, 100 m); because the grid stretches with height, the corresponding mean layer thicknesses below 250 m are 7, 11, 26, 47 and 79 m. Open circles mark the model level heights of each configuration, so the number of levels resolving the rotor can be read directly: 27 at Δz = 5 m falling to 2 at 100 m. Each profile begins at the lowest model level of its own grid and is not extrapolated below it; at Δz = 100 m that level lies at 50 m, above the rotor bottom tip, so the lower-rotor shear is unresolved by construction. The dot-dashed line gives the mean PBLH of the Δz = 5 m reference run for that scheme; the grey band marks the rotor swept zone (30–246 m) and the dotted line the hub height (138 m).

https://doi.org/10.5194/wes-2026-147
Preprint. Discussion started: 10 September 2026

eawe european academy of wind energy
Open Access WIND ENERGY SCIENCE DISCUSSIONS

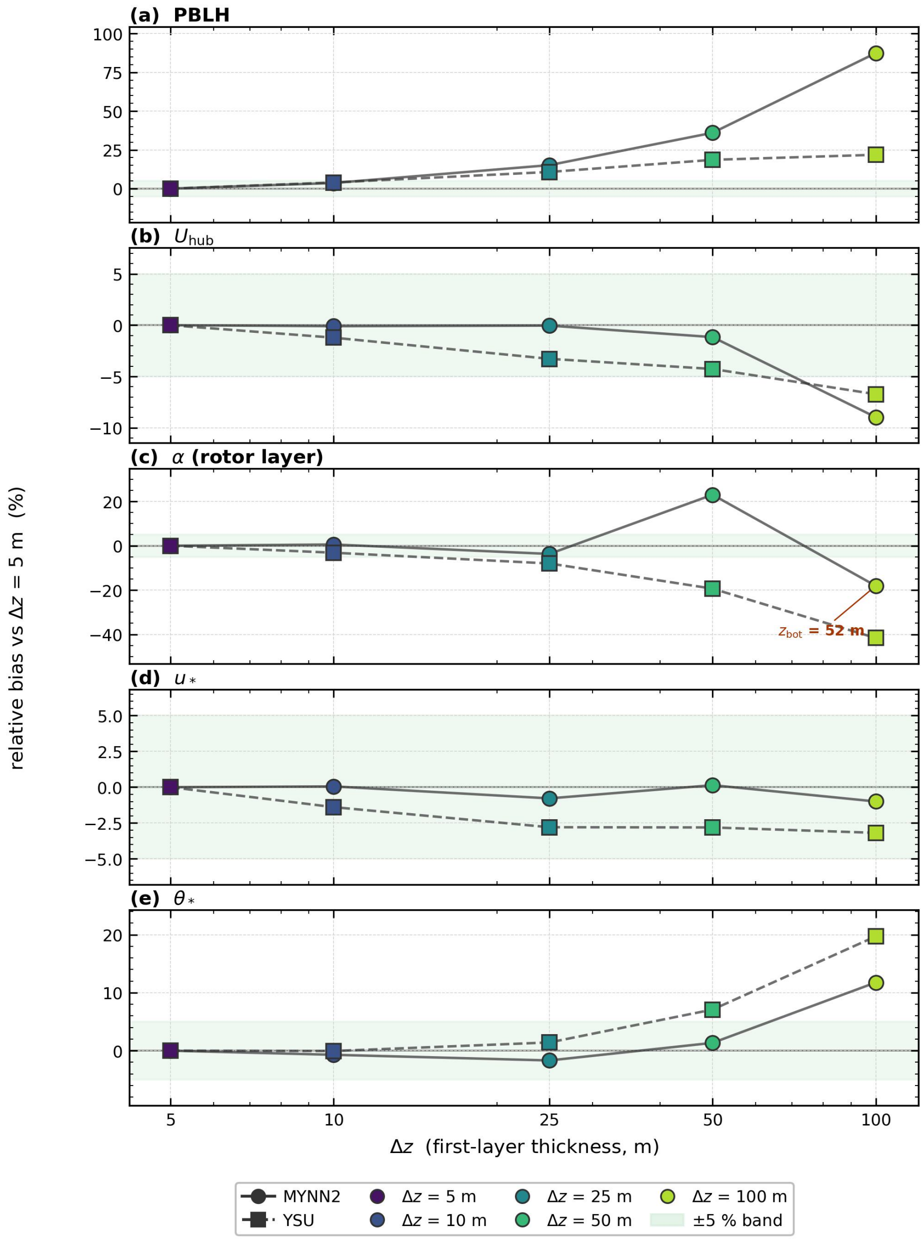

Figure 6. Sensitivity of stable boundary-layer scalars to vertical resolution, for the MYNN2 (circles, solid) and YSU (squares, dashed) schemes. Each panel gives the percentage difference of a diagnostic from its Δz = 5 m value, $(X(\Delta z) - X(\Delta z_5))/|X(\Delta z_5)| \times 100\%$, averaged over stable hours ($z/L > 0.1$) during 2–8 May 2018 as point-hour weighted means: (a) boundary-layer height PBLH; (b) hub-height wind speed $U_{\rm hub}$; (c) wind-shear (power-law) exponent α; (d) friction velocity u_*; (e) surface-layer temperature scale θ_*. Marker colour denotes the configuration, labeled by its first-layer thickness; the grid stretches with height, so Δz is not a uniform spacing. The shaded band marks ±5%. In (c), $\alpha = \ln(U_{\rm top}/U_{\rm bot})/\ln(z_{\rm top}/z_{\rm bot})$ is evaluated between the rotor bottom and top tips (30.5 and 245.5 m) for every configuration except Δz = 100 m, whose lowest model level lies above the bottom tip; there $z_{\rm bot}$ is raised to 52 m, as annotated, and the exponent therefore spans a shallower layer. The Δz = 5 m configuration is the reference throughout; its grid convergence is assessed in the text.

https://doi.org/10.5194/wes-2026-147
Preprint. Discussion started: 10 September 2026

3.2 Spatial structure of the hub-height wake deficit

The time-mean hub-height wake deficit during stable events (Fig. 7) reveals a spatially coherent perturbation field whose structure reflects both the dominant wind direction and the dynamical constraints of the stable MABL characterized in the previous section. The wake emerges sharply at the upwind farm edge and extends as a coherent plume along the prevailing wind direction, with a peak deficit of -3.2 m s^{-1} within the farm footprint and a mean of -2.3 m s^{-1} within 30 km of the cluster centre, the latter about 18% of the co-located no-farm hub-height wind speed of 12.8 m s^{-1} averaged over the same period. Upstream of the farm the deficit averages -0.09 m s^{-1} beyond 100 km, more than an order of magnitude smaller than the in-farm value, as expected given that the Fitch parameterization (for a review of mesoscale wind-farm parameterizations see Fischereit et al., 2022) applies a momentum sink within farm cells without an explicit axial induction term, and therefore cannot represent upstream blockage (Vollmer et al., 2024).

Two features of the spatial structure deserve to be noted. The first is the wake length. Under the stable conditions that dominate the simulation period, the deficit recovers slowly, consistent with the theoretical expectation that suppressed vertical mixing under stable stratification limits the entrainment of momentum from aloft. Along the transect the deficit falls below 0.5 m s^{-1} at 81 km downstream, below 0.25 m s^{-1} at 112 km and below 0.1 m s^{-1} at 136 km. Rosencrans et al. (2024) found wake lengths of approximately 55 km under stable conditions for comparable mid-Atlantic farms, while Pryor et al. (2021) reported that under some flow conditions whole wind-farm wakes, defined by a 5% velocity deficit, extend up to roughly 90 km downwind of the largest US East Coast lease areas for a 15 MW turbine build-out. The longer wake length in the present results reflects the particularly shallow and persistent ABL (118 m, well below hub height), which leaves the upper rotor operating in a layer where turbulent entrainment from aloft to restore momentum to the wake is strongly suppressed.

The second feature is the positive wind speed anomaly flanking the wake at its lateral margins, reaching $+0.35$ m s^{-1} at its strongest, an order of magnitude weaker than the deficit it compensates. This is a mass continuity response: momentum extracted from the farm core accelerates the flow at the lateral boundaries of the momentum deficit region, a feature documented in mesoscale modeling (Fitch et al., 2013) and in long-range scanning lidar measurements combined with mesoscale simulation (Cañadillas et al., 2022). Its presence in the time-mean field confirms that the simulation captures the large-scale dynamical response of the flow to the farm forcing, not merely the local turbine-level deficit. The wakes of other farms along the New Jersey coast are also visible in the domain, though they fall outside the primary analysis region. Their presence underscores the concern raised by Rosencrans et al. (2024) and Porchetta et al. (2024) regarding farm-to-farm interactions under stable stratification, a regime in which the wake of one farm can reach the footprint of a neighboring farm before recovering. Once again, this long wake extent is a result of the stable conditions that are typical to this region in spring and the focus here.

The magnitude of the deficit is itself insensitive to vertical resolution: the transect minimum varies only between -3.2 and -2.6 m s^{-1} across the five configurations, a 20% range against the 13.5:1 range in rotor-layer level count, and the coarsest grid gives the weakest deficit.

https://doi.org/10.5194/wes-2026-147
Preprint. Discussion started: 10 September 2026

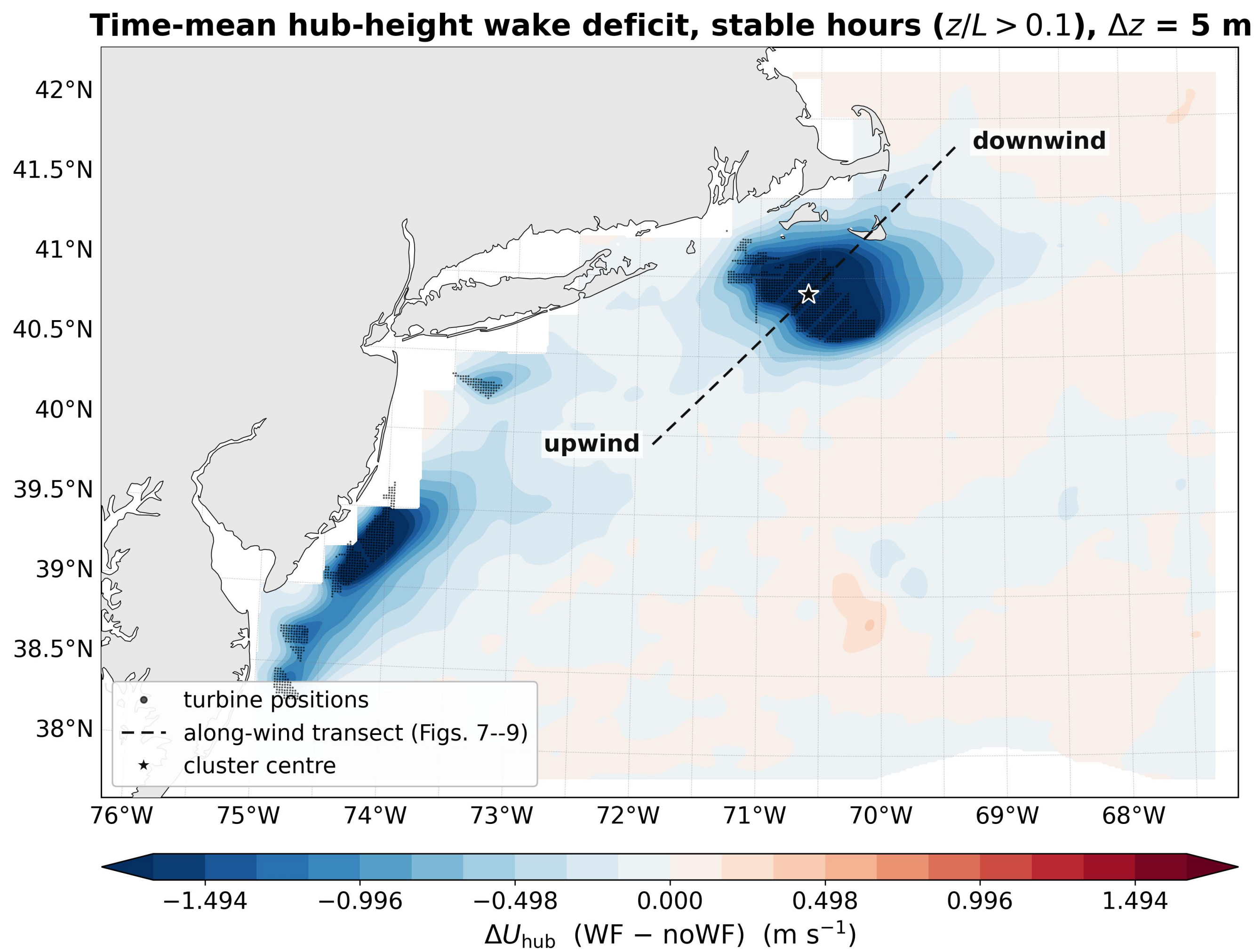

Figure 7. Time-mean hub-height wind-speed deficit (WF−noWF) over the inner domain during stable conditions ($z/L > 0.1$) for the MYNN2 Δz = 5 m configuration, 2–8 May 2018. Colours show the difference in 138 m hub-height wind speed between the wind-farm (WF) and no-farm (noWF) simulations, smoothed with a 5 km Gaussian low-pass filter; blue indicates the wind-speed reduction (wake deficit) over and downwind of the farm, red the compensating acceleration at its lateral margins. Black dots mark turbine positions. The black dashed line is the along-wind (SW–NE) transect through the cluster centre (star) used in Figs. 8, 9 and 10, with its upwind and downwind ends labeled. Stability is classified from the no-farm run at each grid point and hour, so the two simulations are averaged over an identical set of hours.

https://doi.org/10.5194/wes-2026-147
Preprint. Discussion started: 10 September 2026

3.3 Wake deficit and planetary boundary layer perturbation

The four stability regimes in Fig. 8a, c are not separate experiments. Each configuration is a single continuous simulation over 2–8 May 2018 (Sect. 2.2), and stability varies naturally in time through the diurnal and synoptic variability. For each hourly output we compute the lease-area-mean stability z/L from the no-farm run and assign that hour to one of four z/L bins; the box for each bin shows the distribution of hourly lease-mean ΔU_{hub} (or ΔPBLH) over the hours that fell in it. The sample sizes (N) annotated in each panel are hour counts, not run counts. Because each configuration is binned using its own no-farm stability, the counts differ slightly between configurations, by at most three hours in any bin.

The farm-induced perturbations in hub-height wind speed and PBLH are examined through two complementary analyses: their dependence on atmospheric stability across the simulation period (Fig. 8a, c) and their spatial structure along the dominant wind direction (Fig. 8b, d). In every panel the five vertical configurations are shown separately, so that the resolution at which the response departs from the reference is visible directly rather than as an envelope.

The hub-height wind speed deficit (Fig. 8a) is negative across all stability bins and all vertical resolutions, confirming a robust and consistent wake signal throughout the simulation period. At the reference resolution the median deficit is $-0.31\ \mathrm{m\,s^{-1}}$ under near-neutral conditions, $-0.29\ \mathrm{m\,s^{-1}}$ weakly stable, $-0.29\ \mathrm{m\,s^{-1}}$ moderately stable and $-0.21\ \mathrm{m\,s^{-1}}$ strongly stable. The weakening in the most stable bin may reflect lower absolute ambient wind speeds associated with strong stratification, resulting in reduced absolute momentum extraction by the turbines. Overall, the modest gradient across the first three bins should not be interpreted as evidence that stability weakly controls wake deficits; rather, it reflects the limited stability range sampled. The SNE lease area in May is quasi-continuously stable: over the simulated window the lease-area-mean z/L exceeds 0.1 for 80% of hours (Sect. 2.2), and what is labeled 'near-neutral' is in practice weakly stable. The absence of convective events in the dataset collapses the dynamic range that would otherwise reveal a sharper contrast, as documented in year-long simulations over the same region where stability dependence is far more pronounced (Rosencrans et al., 2024; Quint et al., 2025b). The spread across resolutions is modest in the three least stable bins, where the median varies by at most $0.06\ \mathrm{m\,s^{-1}}$, and largest in the strongly stable bin, where it spans -0.21 to $-0.12\ \mathrm{m\,s^{-1}}$. We note that $N \leq 11$ in the moderately stable bin for every configuration and that this bin should be interpreted with caution.

The PBLH perturbation (Fig. 8c) shows a physically coherent transition across stability bins, and at the reference resolution it changes sign. Under near-neutral conditions the farm raises the PBLH by a median of $+4.3$ m through TKE injection into the rotor layer, consistent with the Fitch scheme's representation of turbine-induced mechanical mixing (Fitch et al., 2013). The median response falls to $+2.5$ m in the weakly stable bin and becomes slightly negative in the moderately and strongly stable bins, at -0.5 and -0.2 m, with interquartile ranges spanning zero. Under sufficiently strong stratification the buoyancy restoring force therefore not merely mutes the turbine-induced deepening but can reverse it. The magnitude of this response is known to depend on how much TKE the parameterization adds: Quint et al. (2025a) showed over the same lease area that simulated boundary-layer and surface-temperature impacts vary systematically with the prescribed turbine-added TKE. The response is also markedly more resolution-sensitive than the wind deficit: in the strongly stable bin the median ranges from

https://doi.org/10.5194/wes-2026-147
Preprint. Discussion started: 10 September 2026

-0.2 m at Δz = 5 m to $+4.3$ m at the coarsest grid, so a coarse grid can reverse the sign of the diagnosed response. This is a direct consequence of the PBLH resolution sensitivity identified in Sect. 3.1.

The along-wind transect profiles resolve the spatial structure of these perturbations under stable conditions. The hub-height deficit (Fig. 8b) is negligible upstream, as expected given that the Fitch parameterization represents no upstream induction. The deficit intensifies sharply at the upwind farm edge, reaches a minimum of -3.2 m s^{-1} close to the farm centre, and recovers to a tenth of that value over 93 km downstream. The five configurations track one another closely throughout, the transect minimum spanning -3.2 to -2.6 m s^{-1}, so this spatial structure is insensitive to vertical resolution across the full range tested. Wake deficits of this magnitude and spatial extent under stable offshore conditions are broadly consistent with the observational and modeling literature for the US East Coast and North Sea regions (Cañadillas et al., 2022; Rosencrans et al., 2024), and with the finding that wake extent over this lease area scales with boundary layer depth, suppressed vertical entrainment sustaining the deficit over long downstream distances (Quint et al., 2025a).

The PBLH transect (Fig. 8d) exhibits a dipole structure that is the most spatially distinctive feature of the farm's atmospheric footprint. Inside the farm the PBLH increases by 90 m at the reference resolution, driven by the direct TKE injection of the Fitch scheme. A shallower negative lobe is present on the upwind side (~ -12 m), and immediately downstream of the downwind edge the PBLH undershoots by 24 m. In this wake region, where turbine-injected TKE is absent and background mechanical mixing is reduced, the stable boundary layer re-establishes itself more shallowly than in the undisturbed flow. The perturbation is also far more localised than the wind deficit, recovering to a tenth of its peak within 23 km downstream against 93 km for ΔU_{hub}. The deepening is consistent with the idealized wind-farm simulations of Fitch et al. (2013) and with observational evidence, albeit onshore: Abraham et al. (2025) reported a clear increase in PBLH downstream of an operating wind plant under stable conditions during the AWAKEN campaign, strongest when the upstream boundary layer is shallow, the regime that characterizes the SNE lease area in May. Their downstream signal is positive and decays within roughly 20 km, a recovery distance close to the 23 km found here, whereas the present simulations produce a negative downstream lobe over the same range. Whether that undershoot is physical or an artefact of how the Fitch scheme terminates its TKE source at the farm edge cannot be settled without offshore observations.

The amplitude of the dipole is the most resolution-sensitive aspect of the wake's vertical signature, and its dependence is not monotonic. The in-farm peak is 90 m at Δz = 5 m, rises to 100 and 108 m at 10 and 25 m, and falls to 105 and 77 m at 50 and 100 m. Only the coarsest grid, which cannot resolve the rotor layer at all, substantially underestimates the deepening; the intermediate grids overestimate it by up to 20%. Given that the reference PBLH itself carries a grid convergence index of about 13% (Sect. 3.1), differences between the four finest configurations here are at the edge of what the ensemble can resolve, and only the Δz = 100 m result should be regarded as a clear resolution effect. A comparable resolution floor has been identified at the eddy-resolving end: Wise et al. (2026) found that grid spacing of at least 10 m is required for the rotor drag to be represented in stable boundary layer large-eddy simulation.

https://doi.org/10.5194/wes-2026-147
Preprint. Discussion started: 10 September 2026

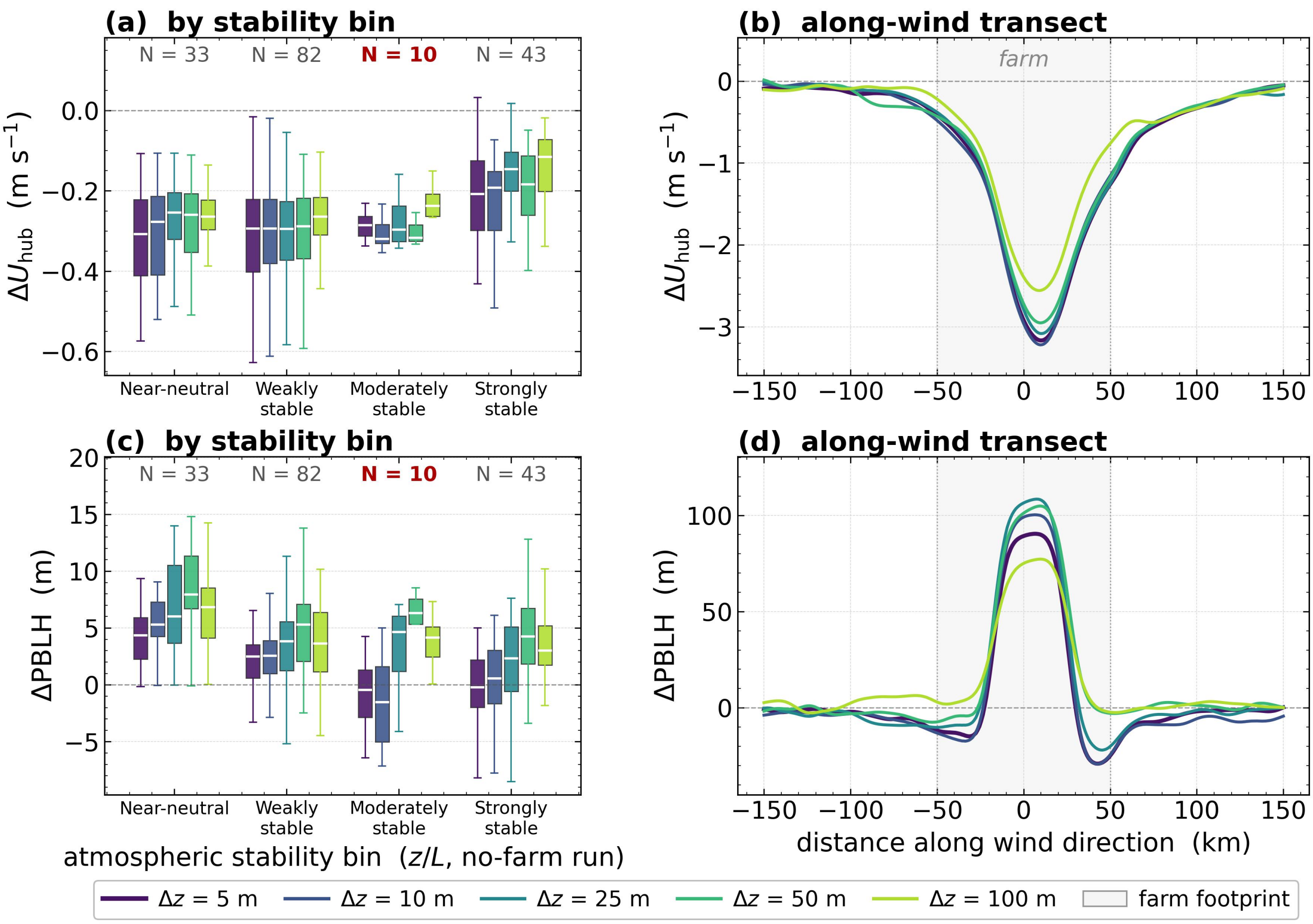

Figure 8. Resolution sensitivity of the wake deficit and boundary-layer response (WF − noWF), MYNN2, 2–8 May 2018. Rows are the two comparators: (a, b) hub-height wind-speed deficit ΔU_{hub} and (c, d) boundary-layer-height change ΔPBLH. (a, c) Distributions grouped by atmospheric stability bin, one box plot per vertical configuration, boxes giving the interquartile range (IQR), whiskers the 1.5 IQR extent and the white line the median; N is the number of hours in each bin, not the number of runs, and is shown in red where fewer than 15 hours contribute. Stability is the lease-area-mean z/L from the no-farm run of each configuration. (b, d) Along-wind transects through the farm under stable conditions ($z/L > 0.1$), one curve per configuration rather than a reference and an envelope, so the resolution at which the response departs is visible directly; the grey band marks the farm footprint. Colour denotes the configuration, labeled by its first-layer thickness. Transect fields use the same 5 km Gaussian low-pass as Figs. 7, 9 and 10 and are sampled by linear interpolation along the wind direction.

https://doi.org/10.5194/wes-2026-147
Preprint. Discussion started: 10 September 2026

eawe european academy of wind energy
Open Access WIND ENERGY SCIENCE DISCUSSIONS

3.4 Ocean mixed layer response and air-sea coupling

The one-dimensional ocean coupled to the atmosphere lets us trace the wind-farm perturbation on the sea surface, without complications of feedbacks from horizontal ocean dynamics: from the mechanical reduction of wind stress, through the shoaling of the ocean mixed layer, to the resulting skin-temperature and air-sea heat-flux response. Figure 9 shows the ocean-state response to a wind-farm (skin temperature ΔT_{SK} and mixed-layer depth ΔH_{ML}) as Δz = 5 m maps (a, c) and along-wind transects (b, d); Figure 10 shows the two bulk air-sea fluxes (momentum flux $\Delta\tau$ and turbulent heat flux $\Delta(\mathrm{HFX}+\mathrm{LH})$) in the same format. All fields are averaged during stable conditions ($z/L > 0.1$) and smoothed with a 5 km Gaussian low-pass, so the transects are cross-section slices consistent with the plan view maps. Farm-zone values quoted below are means within 30 km of the cluster center at the $\Delta z = 5$ m reference resolution.

The mechanical forcing is the reduction in surface wind stress (Fig. 10a, b). Inside the farm the bulk wind stress falls by 1.24×10^{-2} $\mathrm{N\,m^{-2}}$, or 13.5% of the 0.092 $\mathrm{N\,m^{-2}}$ background, and the transect reaches a minimum of -1.51×10^{-2} $\mathrm{N\,m^{-2}}$ just downwind of the cluster centre before recovering over 117 km. This stress deficit is the sea-surface signature of the same momentum extraction that produces the hub-height wake, and its magnitude is consistent with the 30% reduction in wave-supported momentum flux reported for this region by the coupled ocean–atmosphere–wave simulations of Sauvage et al. (2025).

The loss of surface stress due to the turbine weakens wind-driven turbulent mixing in the ocean, and the mixed layer responds by shoaling (Fig. 9c, d). The farm-zone mixed layer is 1.26 m shallower in the WF run than in the noWF run, a reduction of 9.2% relative to the 13.7 m background mixed layer depth, and the transect deepens this shoaling to -1.97 m near the cluster centre, recovering to a tenth of that value within 37 km downstream. The sign and structure follow directly from the Pollard–Rhines–Thompson balance (Pollard et al., 1973), in which reduced surface stress lowers the entrainment-driven deepening of the layer against the sub-mixed-layer stratification. The intermediate step is corroborated over this same lease area by Sauvage et al. (2025), who report a 20% reduction in near-surface ocean turbulent kinetic energy accompanying the wake-induced stress deficit. Mixed-layer shoaling under wind-wake forcing of this kind has also been reported in three-dimensional ocean simulations of offshore wind clusters (Christiansen et al., 2022), but here the effect is isolated from amelioration by ocean dynamical feedbacks.

Because the same surface heat input is now distributed over a thinner mixed layer, the skin temperature warms (Fig. 9a, b). The response is a warming-dominated dipole: the transect peaks at $+0.32$ °C near the cluster centre, flanked by a localized cooling lobe on the upwind side, with the perturbation recovering within 30 km downstream. The farm-zone mean warming is smaller and considerably noisier ($+0.11$ °C at Δz = 5 m, varying between zero and $+0.16$ °C across resolutions), because the one-dimensional slab has no horizontal mixing and the skin-temperature difference is speckled at the grid scale over the shelf-break front; the transect peak is the robust quantity and the farm-zone mean is not. The sign and peak amplitude are nonetheless fully consistent with the fully coupled US East Coast simulations of Seo et al. (2025), which report wake-induced sea surface warming of 0.3–0.4°C and a shallower mixed layer driven by precisely this stress-reduction–shoaling mechanism.

https://doi.org/10.5194/wes-2026-147
Preprint. Discussion started: 10 September 2026

WIND ENERGY SCIENCE DISCUSSIONS

The warmer ocean skin temperature completes the sequence through its impact on the turbulent heat flux (Fig. 10c, d). Under the prevailing stable regime of warm continental air over cool shelf water, with a background sea surface temperature of 10.5 °C in the farm zone, the background turbulent heat flux is directed downward into the ocean ($-20.8\ \mathrm{W\,m^{-2}}$). The farm reduces the magnitude of this downward flux by 2.23 $\mathrm{W\,m^{-2}}$, or 10.7%. The transect peak of $+3.18\ \mathrm{W\,m^{-2}}$ occurs some 47 km downwind of the cluster centre, well downstream of the stress minimum at 5 km, and the anomaly persists over more than 100 km. This downstream displacement is expected: the flux anomaly is mediated by the skin temperature, which must first respond to the accumulated stress deficit, so the thermodynamic signal lags the mechanical one in the advective direction. Both the reduced wind speed and the warmer skin act to weaken the downward flux, so this positive anomaly is the thermodynamic counterpart of the mechanical stress deficit, the same upward heat-flux response that Seo et al. (2025) identify as the feedback that destabilizes the marine boundary layer and partially offsets the wake. The sign is that expected within established frameworks for mesoscale air-sea coupling over surface-temperature anomalies (Chelton et al., 2004; Small et al., 2008).

The coupled response is captured at every vertical resolution, but its magnitude is not monotonic in the grid (Figs. 10b, d). Among the four finest configurations the farm-zone stress reduction spans -0.70 to $-1.35 \times 10^{-2}\ \mathrm{N\,m^{-2}}$, the mixed-layer shoaling 1.08 to 1.35 m, and the heat-flux anomaly 1.97 to 2.42 $\mathrm{W\,m^{-2}}$, with no ordered dependence on resolution; the reference is neither the largest nor the smallest in any of the three. The coarsest grid (Δz = 100 m) is a clear outlier, exaggerating every term: the stress reduction rises to $-1.72 \times 10^{-2}\ \mathrm{N\,m^{-2}}$, 39% above the reference and 2.5 times the Δz = 25 m value, the shoaling to 1.74 m and the heat-flux anomaly to 4.13 $\mathrm{W\,m^{-2}}$, 85% above the reference. The exaggeration is a direct consequence of the degraded near-surface wind forcing at coarse vertical resolution documented in Sect. 3.1. The practical implication is that the ocean response is insensitive to vertical resolution over the range a mesoscale modeller would plausibly choose, but is substantially overestimated once the rotor layer ceases to be resolved at all.

The limitations of the configuration should be stated plainly. The one-dimensional Pollard–Rhines–Thompson ocean has no horizontal dimension and therefore cannot represent Ekman pumping at the farm perimeter (Broström, 2008), positive SST–stability feedback, lateral advection, or wave-driven mixing; nor does it represent the scattering of surface waves by the turbine structures themselves (Zhao et al., 2026). In fully coupled simulations these mechanisms amplify the ocean response over seasonal timescales and can produce a net sea surface warming depending on the broader atmospheric feedback (Seo et al., 2025; Christiansen et al., 2022), and where a coastal circulation is present they can redistribute it: Raghukumar et al. (2023) project cross-shore changes in upwelling induced by offshore wind development along the California coast. The present results should therefore be read as a characterization of the sign, spatial structure, and resolution sensitivity of the first-order mechanical-to-thermal coupling.

The horizontal scale of any three-dimensional oceanic response is worth considering, since only one-dimensional processes are represented here. Restratification by Ekman buoyancy advection and submesoscale eddies and fronts might become important as they are for hurricane wakes (Haney et al., 2012). However, due to the shallow mixed layers at this time, the scale of these phenomena will be very small, requiring sub-kilometer resolution (Dong et al., 2020, 2021).

https://doi.org/10.5194/wes-2026-147
Preprint. Discussion started: 10 September 2026

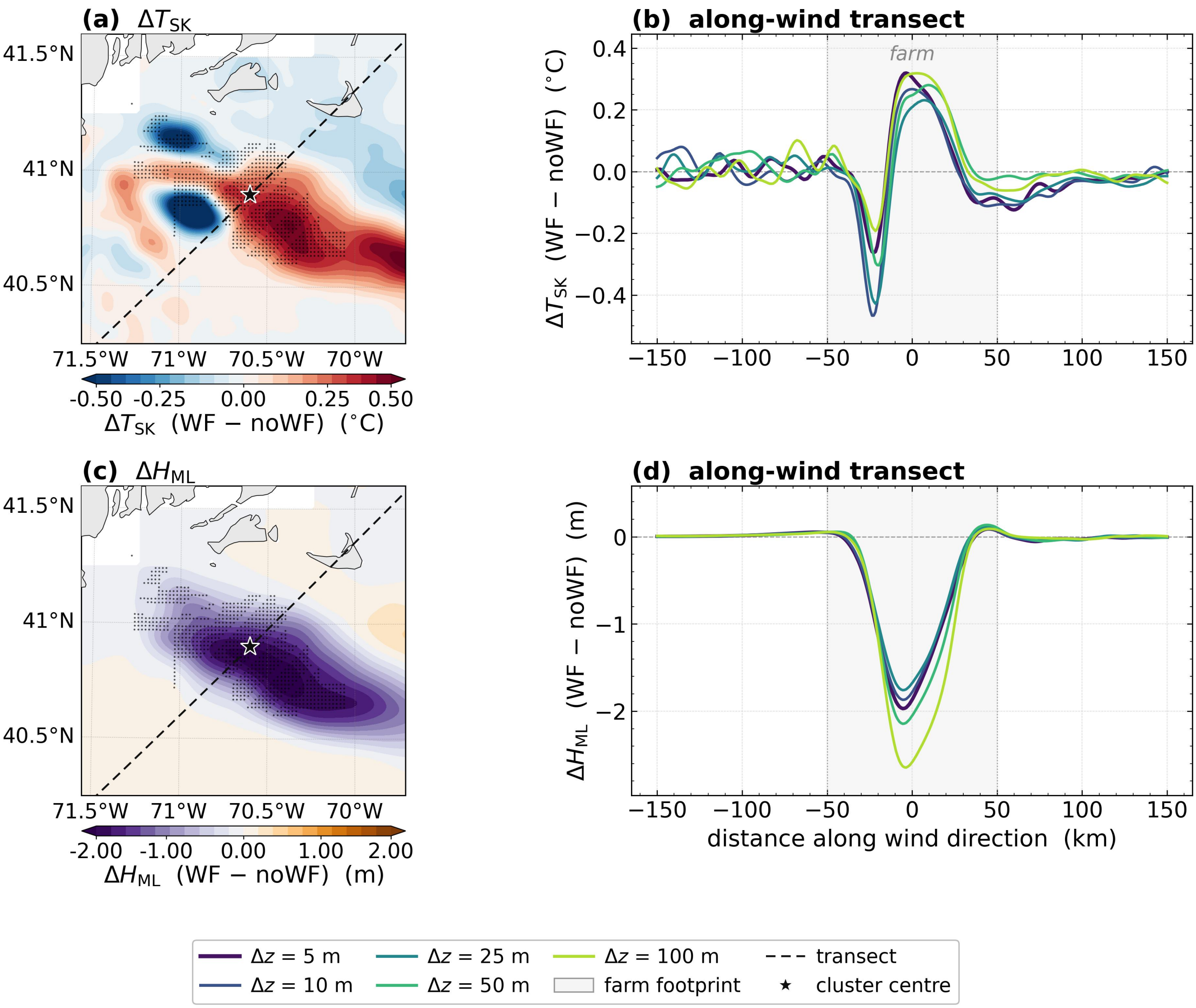

Figure 9. Wind-farm impact on ocean skin temperature and mixed-layer depth (WF − noWF), MYNN2, one-dimensional ocean, stable conditions ($z/L > 0.1$), 2–8 May 2018. Rows are the two fields: (a, b) ΔT_{SK} and (c, d) ΔH_{ML}. (a, c) Δz = 5 m maps, zoomed on the turbine cluster, with the along-wind transect drawn (dashed) through the cluster centre (star); the fine black dots are the individual turbine positions. (b, d) Along-wind transects of the same fields, one curve per vertical configuration rather than a reference and an envelope, so the resolution at which the response departs is visible directly; the grey band marks the farm footprint. Colour denotes the configuration, labeled by its first-layer thickness. All fields are smoothed with a 5 km two-dimensional Gaussian low-pass and the transects are linear slices of those smoothed fields, so the curves are literal cuts through the maps. Stability is classified from the no-farm run at each grid point and hour, so the wind-farm and no-farm runs are averaged over an identical set of hours and the difference of the means equals the mean of the differences. Temperature differences are given in °C; a 1 K and a 1 °C increment are identical.

https://doi.org/10.5194/wes-2026-147
Preprint. Discussion started: 10 September 2026

WIND ENERGY SCIENCE DISCUSSIONS

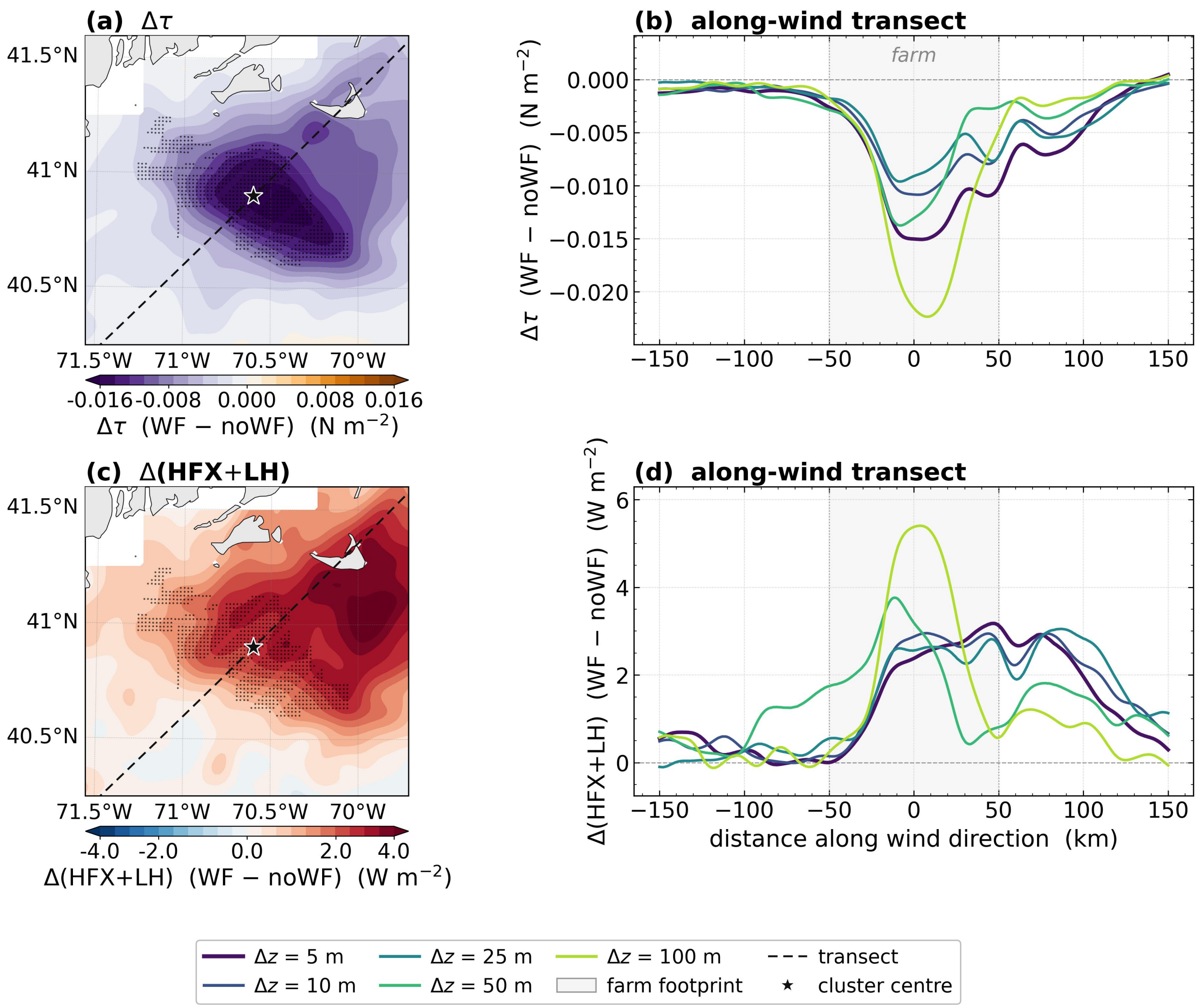

Figure 10. Wind-farm impact on air-sea bulk fluxes (WF − noWF), MYNN2, stable conditions ($z/L > 0.1$), 2–8 May 2018. Rows are the two fluxes: (a, b) the momentum flux (wind stress) $\Delta\tau = \rho C_d\,(U_{10}^2 + V_{10}^2)$, with $\rho = 1.2$ kg m^{-3} and $C_d = 1.2\times10^{-3}$, and (c, d) the turbulent heat flux $\Delta(\mathrm{HFX}+\mathrm{LH})$, positive upward. (a, c) $\Delta z = 5$ m maps, zoomed on the turbine cluster, with the along-wind transect drawn (dashed) through the cluster center (star); the fine black dots are the individual turbine positions. (b, d) Along-wind transects of the same fluxes, one curve per vertical configuration rather than a reference and an envelope, so the resolution at which the response departs is visible directly; the grey band marks the farm footprint. Color denotes the configuration, labeled by its first-layer thickness. Processing matches Fig. 9: a 5 km two-dimensional Gaussian low-pass, with the transects taken as linear slices of the smoothed fields, and stability classified from the no-farm run so that both runs are averaged over an identical set of hours.

https://doi.org/10.5194/wes-2026-147
Preprint. Discussion started: 10 September 2026

4 Conclusions

This study examined the atmospheric and oceanic responses to a large-scale offshore wind farm under the shallow, stable marine boundary layer (MABL) conditions characteristic of the Southern New England (SNE) lease area. Using WRF-Fitch mesoscale simulations across five vertical resolutions and two atmospheric planetary boundary layer (ABL) schemes, we evaluated the sensitivity of wake dynamics and ocean coupling to atmospheric grid discretization. The central findings are synthesized as follows:

– **Rotor-layer decoupling in the stable MABL** (Fig. 5). The stable MABL over the SNE lease area in May is persistently shallow, with a mean boundary layer height (PBLH) of 92 m (YSU) to 118 m (MYNN2). Consequently 59–72% of the rotor swept area sits above the boundary-layer top, and almost all of the shear across the disk is concentrated below hub height. This placement within a strongly stratified layer suppresses vertical mixing and the turbulent redistribution of the wake, driving severe and elongated wind speed deficits, consistent with the finding of Quint et al. (2025a) that wake extent over this same lease area scales with the depth of the boundary layer.

– **Vertical resolution controls the diagnosed boundary-layer depth, not the wake** (Fig. 6). Hub-height wind speed and friction velocity are robustly represented for $\Delta z \leq 50$ m, departing by less than 1.2% and 1% respectively in MYNN2, while PBLH diverges sharply on coarser grids: at $\Delta z = 100$ m, the inability to resolve the sharp stable temperature inversion produces an 87% overestimation in MYNN2 and 22% in YSU. Richardson extrapolation over the three finest grids places most diagnostics within a few per cent of the zero-spacing limit at the reference resolution, but assigns PBLH a grid convergence index of about 13%, so PBLH differences below that threshold should not be read as physical. The wind shear exponent α exhibits a non-monotonic response in MYNN2, peaking at $+23\%$ at $\Delta z = 50$ m; this originates in the lower rotor, where that configuration must interpolate the bottom-tip wind speed across a 25–76 m layer containing no model level, and is distinct in origin from the boundary-layer-top error driving the PBLH bias.

– **Distinctive wake and PBLH spatial signatures** (Figs. 7 and 8). Under stable conditions the time-mean hub-height wake deficit peaks at $-3.2\ \mathrm{m\,s^{-1}}$ at the cluster core and falls below 0.5, 0.25 and 0.1 $\mathrm{m\,s^{-1}}$ at 81, 112 and 136 km downstream. The farm induces a distinct atmospheric dipole, an in-farm PBLH deepening of 90 m followed by a downstream undershoot of 24 m that recovers within 23 km, an order of magnitude more localised than the wind deficit itself. The stability dependence of the PBLH response changes sign: the farm deepens the boundary layer by a median of $+4.3$ m under near-neutral conditions but shoals it slightly under moderate and strong stratification. The in-farm deepening is consistent with the downstream PBLH increases observed onshore during the AWAKEN campaign (Abraham et al., 2025), while the downstream undershoot remains a simulated feature awaiting observational confirmation.

– **Ocean mixed-layer and air-sea coupling** (Figs. 9 and 10). The 1D Pollard–Rhines–Thompson ocean reproduces a coherent mechanical-to-thermal response. The farm reduces the farm-zone surface wind stress by 13.5%, shoaling the ocean mixed layer by 9.2% (1.26 m in the farm-zone mean, reaching -1.97 m along the transect). Concentrating the surface heat input in a thinner layer warms the sea-surface skin (a warming-dominated dipole peaking at $+0.32$ °C)

https://doi.org/10.5194/wes-2026-147
Preprint. Discussion started: 10 September 2026

WIND ENERGY SCIENCE DISCUSSIONS

and drives an upward turbulent heat-flux anomaly of 2.23 $\mathrm{W\,m^{-2}}$, or 10.7%, that weakens the background downward flux of the stable regime; the flux anomaly peaks some 47 km downwind of the stress minimum, reflecting the time the skin temperature takes to respond. Both the sign and the magnitude of this response are consistent with fully coupled simulations of the same region (Seo et al., 2025; Sauvage et al., 2025). The response shows no ordered dependence on resolution among the four finest configurations, but the coarsest grid exaggerates every term, raising the stress reduction by 39% and the heat-flux anomaly by 85% relative to the reference.

– **Vertical refinement is bounded by the horizontal closure** (Table 1). The finest configuration combines a 2.5 m first layer with 1.5 km horizontal spacing, an aspect ratio of order 10^3. At such ratios the vertical grid is no longer the limiting approximation. The ABL schemes used here are one-dimensional column closures, which assume horizontal homogeneity within a grid cell and parameterize vertical fluxes alone; that assumption is already marginal at 1.5 km, within the grey zone in which the energy-containing eddies of the boundary layer are neither fully resolved nor entirely subgrid. Refining the vertical grid sharpens gradients that the horizontal discretization and the closure cannot respond to, and the diminishing returns evident here between Δz = 5 and 10 m, where most diagnostics differ by less than 1%, are consistent with that limit having been reached. The near-surface refinement is additionally constrained from below by the vertical Courant condition on the 7.5 km outer domain (Sect. 2.3), so the achievable resolution is set by the coarser domain rather than the finer one. Progress beyond this point requires relaxing the closure rather than refining the grid: three-dimensional PBL schemes, which represent horizontal as well as vertical mixing (Rybchuk et al., 2022), or large-eddy simulation, in which the energy-containing eddies are resolved and the wake is not parameterized at all. That path carries its own resolution floor, of order 10 m for rotor drag to be represented in the stable boundary layer (Wise et al., 2026). The present results should therefore be read as establishing the vertical resolution required to make full use of a one-dimensional closure at kilometer-scale horizontal resolution, further vertical refinement alone does not improve the solution.

– **The choice of turbulence scheme is often as consequential as resolution** (Fig. 10). The difference between the MYNN2 and YSU schemes are of a similar order to the difference between the finest and coarsest resolutions. Their rate of convergence with resolution differs: typically MYNN2 converged faster than YSU. Furthermore, these schemes showed very different behavior with coarsening, indicating that the choice of scheme becomes more pronounced at marginal resolutions.

Because the 1D slab configuration lacks mechanisms such as Ekman pumping and horizontal advection, the ocean responses documented here represent a conservative lower bound on the farm's true oceanic impact. Extending this framework to fully coupled three-dimensional models (Seo et al., 2025) across the complete seasonal cycle, particularly the convective autumn and winter regimes in which the air-sea heat flux reverses sign, is a critical next step toward a full stability-dependent characterization of offshore wind farm impacts. A complementary direction is to reduce the horizontal grid spacing alongside the vertical, either into the grey zone with a three-dimensional closure or below it with large-eddy simulation, so that the anisotropy

https://doi.org/10.5194/wes-2026-147
Preprint. Discussion started: 10 September 2026

eawe european academy of wind energy
Open Access WIND ENERGY SCIENCE DISCUSSIONS

of the present configuration is relaxed rather than accepted; the cluster and internal wake effects recovered by the latter differ systematically from their mesoscale counterparts off this coast (Sanchez-Gomez et al., 2026).

Code and data availability. All WRF namelists, turbine configuration files, lease-area shapefiles, figure and analysis scripts, and the processed data underlying Figs. 4–10 and Table 1 are archived together at Zenodo (https://doi.org/10.5281/zenodo.21968332). The ASIT direct covariance flux dataset shown in Fig. 1 is available from https://doi.org/10.26025/1912/69658 (Chang and Kirincich, 2025); the ASFB observations in the same figure were provided by N. Laxague.

Author contributions. **AA:** Writing – original draft, formal analysis, methodology, conceptualization, visualization; **BFK:** Writing – review and editing, methodology, conceptualization, supervision, funding acquisition; **NJML:** Writing – review and editing, conceptualization, data curation; funding acquisition; **NP:** Writing – review and editing, conceptualization, data curation, funding acquisition.

Competing interests. The authors declare that they have no known competing financial interests or personal relationships that could have appeared to influence the work reported in this paper.

Acknowledgements. Computations were performed using Brown University's resources on OSCAR; we thank Dr. Paul Hall (OSCAR and CCV support) for assistance with computing workflows and troubleshooting. B. Fox-Kemper and A. Ayouche were partially supported by a RI Science and Technology Advisory Council award and US Department of Energy grant DE-SC0024572. N. Laxague was supported by the US Department of Energy grant DE-SC0024572. N. Pizzo was supported by a RI Science and Technology Advisory Council award.

https://doi.org/10.5194/wes-2026-147
Preprint. Discussion started: 10 September 2026

WIND ENERGY SCIENCE DISCUSSIONS

References

Abraham, A., Puccioni, M., Jordan, A., Maric, E., Bodini, N., Hamilton, N., Letizia, S., Klein, P. M., Smith, E. N., Wharton, S., Gero, J., Jacob, J. D., Krishnamurthy, R., Newsom, R. K., Pekour, M., Radünz, W., and Moriarty, P.: Operational wind plants increase planetary boundary layer height: an observational study, Wind Energy Science, 10, 1681–1705, https://doi.org/10.5194/wes-10-1681-2025, 2025.

Angevine, W. M., Hare, J. E., Fairall, C. W., Wolfe, D. E., Hill, R. J., Brewer, W. A., and White, A. B.: Structure and formation of the highly stable marine boundary layer over the Gulf of Maine, Journal of Geophysical Research: Atmospheres, 111, https://doi.org/10.1029/2006JD007465, 2006.

Archer, C. L., Wu, S., Ma, Y., and Jiménez, P. A.: Two corrections for turbulent kinetic energy generated by wind farms in the WRF model, Monthly Weather Review, 148, 4823–4835, https://doi.org/10.1175/MWR-D-20-0097.1, 2020.

Bodini, N., Lundquist, J. K., and Kirincich, A.: U.S. East Coast lidar measurements show offshore wind turbines will encounter very low atmospheric turbulence, Geophysical Research Letters, 46, 5582–5591, https://doi.org/10.1029/2019GL082636, 2019.

Bodini, N., Optis, M., Redfern, S., Rosencrans, D., Rybchuk, A., Lundquist, J. K., Pronk, V., Castagneri, S., Purkayastha, A., Draxl, C., Krishnamurthy, R., Young, E., Roberts, B., Rosenlieb, E., and Musial, W.: The 2023 National Offshore Wind data set (NOW-23), Earth System Science Data, 16, 1965–2006, https://doi.org/10.5194/essd-16-1965-2024, 2024.

Broström, G.: On the influence of large wind farms on the upper ocean circulation, Journal of Marine Systems, 74, 585–591, https://doi.org/10.1016/j.jmarsys.2008.05.001, 2008.

Cañadillas, B., Beckenbauer, M., Trujillo, J. J., Dörenkämper, M., Foreman, R., Neumann, T., and Lampert, A.: Offshore wind farm cluster wakes as observed by long-range-scanning wind lidar measurements and mesoscale modeling, Wind Energy Science, 7, 1241–1262, https://doi.org/10.5194/wes-7-1241-2022, 2022.

Chang, Y. and Kirincich, A. R.: Long-term, quality-controlled observations of near-shore wind momentum and heat flux at the Martha's Vineyard Coastal Observatory's Air-Sea Interaction Tower, https://doi.org/10.26025/1912/71935, data set, 2025.

Chelton, D. B., Schlax, M. G., Freilich, M. H., and Milliff, R. F.: Satellite measurements reveal persistent small-scale features in ocean winds, Science, 303, 978–983, https://doi.org/10.1126/science.1091901, 2004.

Chen, F. and Dudhia, J.: Coupling an advanced land surface–hydrology model with the Penn State–NCAR MM5 modeling system. Part I: model implementation and sensitivity, Monthly Weather Review, 129, 569–585, https://doi.org/10.1175/1520-0493(2001)129<0569:CAALSH>2.0.CO;2, 2001.

Christiansen, N., Daewel, U., Djath, B., and Schrum, C.: Emergence of large-scale hydrodynamic structures due to atmospheric offshore wind farm wakes, Frontiers in Marine Science, 9, 818 501, https://doi.org/10.3389/fmars.2022.818501, 2022.

Daewel, U., Akhtar, N., Christiansen, N., and Schrum, C.: Offshore wind farms are projected to impact primary production and bottom water deoxygenation in the North Sea, Communications Earth & Environment, 3, 292, https://doi.org/10.1038/s43247-022-00625-0, 2022.

de Boyer Montégut, C.: Mixed layer depth over the global ocean: a climatology computed with a density threshold criterion of 0.03 kg m^{-3} from the value at the reference depth of 5 m, https://doi.org/10.17882/98226, data set, 2024.

Dong, J., Fox-Kemper, B., Zhang, H., and Dong, C.: The scale of submesoscale baroclinic instability globally, Journal of Physical Oceanography, 50, 2649–2667, https://doi.org/10.1175/JPO-D-20-0043.1, 2020.

Dong, J., Fox-Kemper, B., Zhang, H., and Dong, C.: The scale and activity of symmetric instability estimated from a global submesoscale-permitting ocean model, Journal of Physical Oceanography, 51, 1655–1670, https://doi.org/10.1175/JPO-D-20-0159.1, 2021.

https://doi.org/10.5194/wes-2026-147
Preprint. Discussion started: 10 September 2026

Fischereit, J., Brown, R., Larsén, X. G., Badger, J., and Hawkes, G.: Review of mesoscale wind-farm parametrizations and their applications, Boundary-Layer Meteorology, 182, 175–224, https://doi.org/10.1007/s10546-021-00652-y, 2022.

Fitch, A. C., Olson, J. B., Lundquist, J. K., Dudhia, J., Gupta, A. K., Michalakes, J., and Barstad, I.: Local and mesoscale impacts of wind farms as parameterized in a mesoscale NWP model, Monthly Weather Review, 140, 3017–3038, https://doi.org/10.1175/MWR-D-11-00352.1, 2012.

Fitch, A. C., Lundquist, J. K., and Olson, J. B.: Mesoscale influences of wind farms throughout a diurnal cycle, Monthly Weather Review, 141, 2173–2198, https://doi.org/10.1175/MWR-D-12-00185.1, 2013.

Floeter, J., Pohlmann, T., Harmer, A., and Möllmann, C.: Chasing the offshore wind farm wind-wake-induced upwelling/downwelling dipole, Frontiers in Marine Science, Volume 9 - 2022, https://doi.org/10.3389/fmars.2022.884943, 2022.

García-Santiago, O., Hahmann, A. N., Badger, J., and Peña, A.: Evaluation of wind farm parameterizations in the WRF model under different atmospheric stability conditions with high-resolution wake simulations, Wind Energy Science, 9, 963–979, https://doi.org/10.5194/wes-9-963-2024, 2024.

Haney, S., Bachman, S., Cooper, B., Kupper, S., McCaffrey, K., Van Roekel, L., Stevenson, S., Fox-Kemper, B., and Ferrari, R.: Hurricane wake restratification rates of 1, 2 and 3-dimensional processes, Journal of Marine Research, 70, 824–850, https://doi.org/10.1357/002224012806770937, 2012.

Hawbecker, P., Lassman, W., Juliano, T. W., Kosović, B., and Haupt, S. E.: Model sensitivity across scales: a case study of simulating an offshore low-level jet, Wind Energy Science, 11, 51–69, https://doi.org/10.5194/wes-11-51-2026, 2026.

Hersbach, H., Bell, B., Berrisford, P., Hirahara, S., Horányi, A., Muñoz-Sabater, J., Nicolas, J., Peubey, C., Radu, R., Schepers, D., Simmons, A., Soci, C., Abdalla, S., Abellan, X., Balsamo, G., Bechtold, P., Biavati, G., Bidlot, J., Bonavita, M., De Chiara, G., Dahlgren, P., Dee, D., Diamantakis, M., Dragani, R., Flemming, J., Forbes, R., Fuentes, M., Geer, A., Haimberger, L., Healy, S., Hogan, R. J., Hólm, E., Janisková, M., Keeley, S., Laloyaux, P., Lopez, P., Lupu, C., Radnoti, G., de Rosnay, P., Rozum, I., Vamborg, F., Villaume, S., and Thépaut, J.-N.: The ERA5 global reanalysis, Quarterly Journal of the Royal Meteorological Society, 146, 1999–2049, https://doi.org/10.1002/qj.3803, 2020.

Holtslag, A. A. M., Svensson, G., Baas, P., Basu, S., Beare, B., Beljaars, A. C. M., Bosveld, F. C., Cuxart, J., Lindvall, J., Steeneveld, G. J., Tjernström, M., and van de Wiel, B. J. H.: Stable atmospheric boundary layers and diurnal cycles: challenges for weather and climate models, Bulletin of the American Meteorological Society, 94, 1691–1706, https://doi.org/10.1175/BAMS-D-11-00187.1, 2013.

Hong, S.-Y., Noh, Y., and Dudhia, J.: A new vertical diffusion package with an explicit treatment of entrainment processes, Monthly Weather Review, 134, 2318–2341, https://doi.org/10.1175/MWR3199.1, 2006.

Iacono, M. J., Delamere, J. S., Mlawer, E. J., Shephard, M. W., Clough, S. A., and Collins, W. D.: Radiative forcing by long-lived greenhouse gases: calculations with the AER radiative transfer models, Journal of Geophysical Research: Atmospheres, 113, https://doi.org/10.1029/2008JD009944, 2008.

Jiang, H. and Edson, J. B.: Characteristics and scaling of the stable marine internal boundary layer, Journal of Geophysical Research: Atmospheres, 126, e2021JD035 510, https://doi.org/10.1029/2021JD035510, 2021.

Laxague, N. J. M., Schwadron, J., Duvarci, Z. G., Hickey, E., Shellito, S., and Emond, M.: Observations of air-sea turbulent fluxes and marine atmospheric boundary layer structure from a coastal meteorological buoy, in preparation for Ocean Engineering, 2026.

Lentz, S. J.: Seasonal warming of the Middle Atlantic Bight Cold Pool, Journal of Geophysical Research: Oceans, 122, 941–954, https://doi.org/10.1002/2016JC012201, 2017.

https://doi.org/10.5194/wes-2026-147
Preprint. Discussion started: 10 September 2026

Liu, Y., Gaudet, B., Krishnamurthy, R., Tai, S.-L., Berg, L. K., Bodini, N., Rybchuk, A., and Kumler, A.: Identifying meteorological drivers for errors in modeled winds along the northern California coast, Monthly Weather Review, 152, 455–469, https://doi.org/10.1175/MWR-D-23-0030.1, 2024.

McCoy, A., Musial, W., Hammond, R., Mulas Hernando, D., Duffy, P., Beiter, P., Pérez, P., Baranowski, R., Reber, G., and Spitsen, P.: Offshore wind market report: 2024 edition, Tech. Rep. NREL/TP-5000-90525, National Renewable Energy Laboratory, Golden, CO, USA, https://doi.org/10.2172/2434294, 2024.

Monin, A. S. and Obukhov, A. M.: Basic laws of turbulent mixing in the surface layer of the atmosphere, Contrib. Geophys. Inst. Acad. Sci. USSR, 24, 163–187, 1954.

Nakanishi, M. and Niino, H.: An improved Mellor–Yamada level-3 model with condensation physics: its design and verification, Boundary-Layer Meteorology, 112, 1–31, https://doi.org/10.1023/B:BOUN.0000020164.04146.98, 2004.

Nakanishi, M. and Niino, H.: Development of an improved turbulence closure model for the atmospheric boundary layer, Journal of the Meteorological Society of Japan. Ser. II, 87, 895–912, https://doi.org/10.2151/jmsj.87.895, 2009.

Pareja-Roman, L. F., Miles, T., and Glenn, S.: Coastal upwelling modulates winds and air-sea fluxes, impacting offshore wind energy, Frontiers in Energy Research, 12, 1470 712, https://doi.org/10.3389/fenrg.2024.1470712, 2024.

Pollard, R. T., Rhines, P. B., and Thompson, R. O. R. Y.: The deepening of the wind-mixed layer, Geophysical Fluid Dynamics, 4, 381–404, https://doi.org/10.1080/03091927208236105, 1973.

Porchetta, S., Howland, M. F., Borgers, R., Buckingham, S., and Munters, W.: Annual wake impacts in and between wind farm clusters modelled by a mesoscale numerical weather prediction model and fast-running engineering models, Wind Energy Science Discussions, 2024, 1–37, https://doi.org/10.5194/wes-2024-58, 2024.

Pryor, S. C., Barthelmie, R. J., and Shepherd, T. J.: Wind power production from very large offshore wind farms, Joule, 5, 2663–2686, https://doi.org/10.1016/j.joule.2021.09.002, 2021.

Quint, D., Lundquist, J. K., Bodini, N., and Rosencrans, D.: Simulated meteorological impacts of offshore wind turbines and sensitivity to the amount of added turbulence kinetic energy, Wind Energy Science, 10, 1269–1301, https://doi.org/10.5194/wes-10-1269-2025, 2025a.

Quint, D., Lundquist, J. K., and Rosencrans, D.: Simulations suggest offshore wind farms modify low-level jets, Wind Energy Science, 10, 117–142, https://doi.org/10.5194/wes-10-117-2025, 2025b.

Raghukumar, K., Nelson, T., Jacox, M., Chartrand, C., Fiechter, J., Chang, G., Cheung, L., and Roberts, J.: Projected cross-shore changes in upwelling induced by offshore wind farm development along the California coast, Communications Earth & Environment, 4, 1–12, https://doi.org/10.1038/s43247-023-00780-y, 2023.

Rosencrans, D., Lundquist, J. K., Optis, M., Rybchuk, A., Bodini, N., and Rossol, M.: Seasonal variability of wake impacts on US mid-Atlantic offshore wind plant power production, Wind Energy Science, 9, 555–583, https://doi.org/10.5194/wes-9-555-2024, 2024.

Rybchuk, A., Juliano, T. W., Lundquist, J. K., Rosencrans, D., Bodini, N., and Optis, M.: The sensitivity of the Fitch wind farm parameterization to a three-dimensional planetary boundary layer scheme, Wind Energy Science, 7, 2085–2098, https://doi.org/10.5194/wes-7-2085-2022, 2022.

Sanchez-Gomez, M., Deskos, G., Optis, M., Lundquist, J. K., Sinner, M., Xia, G., and Musial, W.: Differences in cluster and internal wake effects from mesoscale and large-eddy simulations off the US East Coast, Wind Energy Science, 11, 2009–2036, https://doi.org/10.5194/wes-11-2009-2026, 2026.

Sauvage, C., Seo, H., Zippel, S., Clayson, C. A., and Edson, J. B.: Fetch-dependent surface wave responses to offshore wind farms in the northeast U.S. coast, Journal of Geophysical Research: Oceans, 130, e2025JC023 156, https://doi.org/10.1029/2025JC023156, 2025.

https://doi.org/10.5194/wes-2026-147
Preprint. Discussion started: 10 September 2026

Seo, H., Sauvage, C., Renkl, C., Lundquist, J. K., and Kirincich, A.: Sea surface warming and ocean-to-atmosphere feedback driven by large-scale offshore wind farms under seasonally stratified conditions, Science Advances, 11, eadw7603, https://doi.org/10.1126/sciadv.adw7603, 2025.

Shaw, W. J., Berg, L. K., Cline, J., Draxl, C., Djalalova, I., Grimit, E. P., Lundquist, J. K., Marquis, M., McCaa, J., Olson, J. B., Sivaraman, C., Sharp, J., and Wilczak, J. M.: Scientific challenges to characterizing the wind resource in the marine atmospheric boundary layer, Wind Energy Science, 7, 2307–2334, https://doi.org/10.5194/wes-7-2307-2022, 2022.

Skamarock, W. C., Klemp, J. B., Dudhia, J., Gill, D. O., Liu, Z., Berner, J., Wang, W., Powers, J. G., Duda, M. G., Barker, D. M., and Huang, X.-Y.: A description of the Advanced Research WRF Model version 4, NCAR Tech. Note NCAR/TN-556+STR, National Center for Atmospheric Research, Boulder, CO, USA, https://doi.org/10.5065/1dfh-6p97, 2019.

Small, R. J., deSzoeke, S. P., Xie, S. P., O'Neill, L., Seo, H., Song, Q., Cornillon, P., Spall, M., and Minobe, S.: Air–sea interaction over ocean fronts and eddies, Dynamics of Atmospheres and Oceans, 45, 274–319, https://doi.org/10.1016/j.dynatmoce.2008.01.001, 2008.

Svensson, G. and Holtslag, A. A. M.: Analysis of model results for the turning of the wind and related momentum fluxes in the stable boundary layer, Boundary-Layer Meteorology, 132, 261–277, https://doi.org/10.1007/s10546-009-9395-1, 2009.

Taylor, K. E.: Summarizing multiple aspects of model performance in a single diagram, Journal of Geophysical Research: Atmospheres, 106, 7183–7192, https://doi.org/10.1029/2000JD900719, 2001.

Thompson, G., Field, P. R., Rasmussen, R. M., and Hall, W. D.: Explicit forecasts of winter precipitation using an improved bulk microphysics scheme. Part II: implementation of a new snow parameterization, Monthly Weather Review, 136, 5095–5115, https://doi.org/10.1175/2008MWR2387.1, 2008.

Veers, P., Dykes, K., Basu, S., Bianchini, A., Clifton, A., Green, P., Holttinen, H., Kitzing, L., Kosović, B., Lundquist, J. K., Meyers, J., O'Malley, M., Shaw, W. J., and Straw, B.: Grand challenges: wind energy research needs for a global energy transition, Wind Energy Science, 7, 2491–2496, https://doi.org/10.5194/wes-7-2491-2022, 2022.

Vollmer, L., Sengers, B. A. M., and Dörenkämper, M.: Brief communication: A simple axial induction modification to the Weather Research and Forecasting Fitch wind farm parameterization, Wind Energy Science, 9, 1689–1693, https://doi.org/10.5194/wes-9-1689-2024, 2024.

Wind Forecast Improvement Project 3: WFIP3 lidar wind profile observations at Block Island, Rhode Island, https://doi.org/10.21947/3014087, data set, 2025.

Wise, A. S., Arthur, R. S., Mirocha, J. D., Lundquist, J. K., and Chow, F. K.: Idealized simulations of wind farm interactions with intermittent turbulence in stable boundary layer conditions, Wind Energy Science, 11, 2543–2565, https://doi.org/10.5194/wes-11-2543-2026, 2026.

Zhao, B. et al.: A subgrid-scale parameterization of wave-structure interactions for spectral wave models: idealized simulations in offshore wind farm conditions, Journal of Advances in Modeling Earth Systems, https://doi.org/10.1029/2025MS005603, 2026.